BIOMEDICAL ENGINEERING

Automated Passive Marker Tracking for MR-Guided Endovascular Interventions

A.E. ter Braak

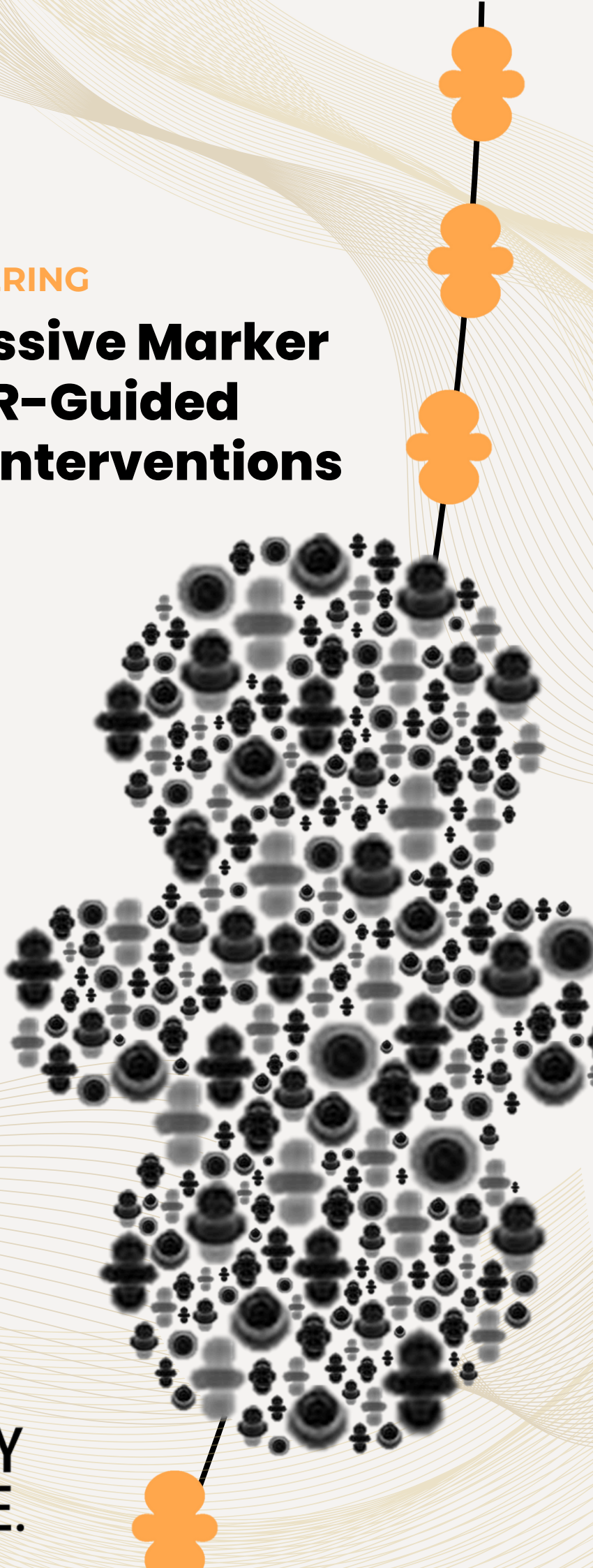

MD&I
UNIVERSITY OF TWENTE.

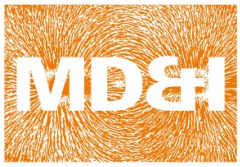

UNIVERSITY OF TWENTE. | TECHMED CENTRE

Faculty of Science and Technology,
Medical Detection and Imaging,
Biomedical Engineering

Master thesis

-

Automated Passive Marker Tracking for MR-Guided Endovascular Interventions

---

Author A.E. ter Braak

Chair Prof.Dr.Ir. B. ten Haken

Magnetic Detection & Imaging group, University of Twente.

Leading Supervisor Dr.Ir. W.M. Brink

Magnetic Detection & Imaging group, University of Twente.

External Supervisor Dr. E. Groot Jebbink

Multi-Modality Medical Imaging group, University of Twente.

11-04-2025

Abstract

EN:
Endovascular interventions provide a less invasive alternative to open surgery, generally guided by fluoroscopy, which exposes clinical staff and patients to ionizing radiation. Magnetic resonance imaging (MRI) offers a promising alternative, providing image guidance in any possible position and plane orientation, with excellent soft tissue contrast and free of ionizing radiation. However, the application of MRI guidance in endovascular interventions is still limited by challenges the visualization and tracking of the guidewire.

This thesis addresses these challenges by developing an automated passive marker tracking algorithm for interventional MRI (iMRI) suites, using a deep learning based detection approach combined with slice repositioning. The convolutional neural network (CNN) is trained with simulated representations of passive markers, which reduces the dependency on gaining extensive training data. The CNN automatically detects passive markers on real MR-images. The final solution combines the output from the CNN with a slice repositioning algorithm, and enables automated 3D passive marker tracking with a high accuracy.

NL:
Endovasculaire interventies bieden een minder invasief alternatief voor open chirurgie, meestal geleid door fluoroscopie, waarbij klinisch personeel en patiënten worden blootgesteld aan ioniserende straling. Magnetic resonance imaging (MRI) biedt een veelbelovend alternatief, met beeldbegeleiding mogelijk in elke positie en oriëntatie, met uitstekend zachtweefselcontrast en zonder ioniserende straling. De toepassing van MRI-begeleiding bij endovasculaire interventies wordt echter nog steeds beperkt door uitdagingen op het gebied van de visualisatie en het volgen van de voerdraad.

In dit scriptie onderzoek worden deze uitdagingen aangepakt door een algoritme voor het automatisch volgen van passieve markers te ontwikkelen voor interventionele MRI-suites (iMRI). Hierbij wordt gebruik gemaakt van deep learning voor marker detectie in combinatie met herpositionering van de slice. Het convolutionele neurale netwerk (CNN) wordt getraind met gesimuleerde representaties van passieve markers, waardoor men minder afhankelijk is van het verkrijgen van uitgebreide trainingsgegevens uit de kliniek. De CNN detecteert automatisch passieve markers op echte MR-beelden. De uiteindelijke oplossing combineert de output van de CNN met een algoritme voor het herpositioneren van de slices en maakt het automatisch volgen van passieve markers in 3D met een hoge nauwkeurigheid mogelijk.

Acknowledgment

This thesis presents my graduation assignment, titled "*Automated passive marker tracking for MR-guided endovascular interventions*", performed within the Magnetic Detection & Imaging research group at the University of Twente.

I would like to thank my supervisors for their guidance during my master's thesis. A special thanks to my leading supervisor, Wyger Brink, for his guidance, sharp insights and constructive feedback throughout my assignment. Our weekly meetings were always motivating and it was nice to work with someone who shared my excitement about scanning small paramagnetic rings with the MRI. I really enjoyed my time working on a solution for automated 3D passive marker tracking for iMRI, so thank you for giving me the opportunity.

To my amazing boyfriend: thank you for your constant support and occasionally being my personal barista (serving the best coffee in Enschede). Another big thank you to my family for their support. I appreciate how you have patiently listened to my thesis updates (and then listened again when I kept showing more images during the process).

I am also grateful to my friends for the weekly dinners and conversations, which I really enjoyed after a day of work. And to my fellow master's students: Thanks a lot for the caffeine-fueled couch talks in the TechMed Centre and, of course, the spontaneous meme dumps that kept the vibes alive.

With this thesis, my study in Biomedical Engineering at the University of Twente comes to an end. I really enjoyed my time as a student, but the next adventures are just getting started and I am looking forward to it!

Anieck ter Braak
Enschede, April 2025

List of Acronyms

AAA	abdominal aortic aneurysm
AI	artificial intelligence
bSSFP	balanced steady-state free precession
CNN	convolutional neural network
CNR	contrast-to-noise ratio
FN	false negatives
FOV	field of view
FP	false positives
FSE	fast spin echo
GRE	gradient recalled echo
iMRI	interventional MRI
MR	magnetic resonance
MRI	magnetic resonance imaging
RF	radio frequency
RMSE	root-mean-square error
SNR	signal-to-noise ratio
T1	longitudinal relaxation
T2	transverse relaxation
TE	echo time
TP	true positives
TR	repetition time

Contents

1 Introduction

Endovascular interventions guided by imaging techniques provide a less invasive treatment and a faster recovery compared to open surgery [1, 2]. Endovascular interventions are therefore used for many clinical application and often involve guiding a guidewire to a desired position within the vasculature. This is traditionally performed under fluoroscopic image-guidance, combined with intravenous injections of iodinated contrast agents to visualize the vasculature. Fluoroscopy offers a relatively high frame rate dynamic imaging for endovascular interventions, but it does expose patients and in particular clinical staff to ionizing radiation [3]. Although clinical staff aims to minimize their exposure, complex and prolonged procedures still contribute significantly to high levels of exposure for interventional procedures [4].

The use of magnetic resonance imaging (MRI) for endovascular procedures has gained increasing interest from the community recently, with the commercial introduction of low-field high-performance systems with increased bore diameter, offering increased access and robustness for interventional procedures [5]. interventional MRI (iMRI) offers imaging in any image plane orientation, provides excellent soft tissue contrast and does not use ionizing radiation. Building on efficient real-time imaging sequences, iMRI could also offer potential benefits during endovascular procedures, such as guiding a catheter with a guidewire. These guidance procedures depends on precise and real-time visualization and tracking of the guidewire. Since guidewires are not inherently visible with MRI, specialized techniques are needed for accurate visualization and tracking of guidewires with MRI.

For guidewire tracking, marker-based approaches are often applied for the localization of the guidewire with iMRI. The guidewires contain embedded markers that can be categorized as active or passive markers [6, 7]. Active markers are often micro coils that signal the precise location of the marker, which requires additional specialized equipment and thicker guidewires. In contrast, passive tracking relies on visual detection of passive markers in the scanned magnetic resonance (MR) images. As no additional hardware is needed, passive tracking is therefore more appealing and easier to implement in the iMRI suite. A study of Reinok et al. has shown the potential of passive guidewire tracking with iMRI based on 2D marker detection in a real-time imaging sequence [8]. This thesis aims to optimize the performance of the automated 2D detection and introduce 3D tracking to improve the feasibility of automated 3D passive guidewire tracking for an iMRI system. To achieve this, this thesis addresses three primary objectives: the simulation of passive marker susceptibility artifacts, developing deep learning methods for automated 2D marker detection and tracking markers real-time in 3D. Chapter 2 provides relevant background information on iMRI for endovascular procedures. The research objectives and approach are highlighted in Chapter 3. Chapter 4 addresses the simulation of susceptibility artifacts and their appearances in MR images. Chapter 5 presents deep learning methods for automated 2D detection, where chapter 6 presents a solution for automated 3D passive marker tracking in real time with slice repositioning. The final insights and future perspectives are discussed in Chapter 7, followed by overall conclusions in Chapter 8.

2 | Background

This chapter explores the relevant context in which this thesis will be conducted. By examining the clinical and technical aspects to guide endovascular interventions with iMRI, a deeper understanding of the research problem is formed. It will provide relevant background information and supports the motivation behind this thesis.

2.1 Endovascular interventions

Endovascular interventions are minimally invasive procedures that treat various vascular diseases, such as abdominal aortic aneurysm (AAA) or peripheral artery disease. By inserting catheters into the vasculature through small incisions, diseases can be assessed from the inside instead of performing open surgery. These interventions are guided by imaging modalities ensuring precise navigation during endovascular procedures. The benefits of endovascular interventions include faster recovery and less invasive treatment for patients [1, 2]. For example, AAA can be treated with an endovascular aneurysm repair, where a stent graft is placed inside the aorta to prevent aneurysm rupture. Compared to open surgery for aneurysm repair, endovascular repair show superior patient outcomes [9].

2.2 Magnetic resonance imaging

MRI is a medical imaging technique used to image human anatomy and physiology. It is often used for diagnostic purposes and treatment monitoring. Unlike X-rays, PET or CT-scans, MRI does not use ionizing radiation, as it uses a magnetic field, typically ranging from 1.5 to 3 Tesla for most systems. While these fields are generally save, contraindications for MR are presence of metallic implants due to safety risks associated with interactions between the magnetic fields and the implant.

MRI imaging is based on the *spin* property of certain atomic nuclei, the most commonly used being hydrogen [10]. MRI involves a strong external magnetic field ($\boldsymbol{B_0}$), radio frequency (RF) pulses and magnetic field gradients to elicit a signal from these nuclei and form an image. During MRI, $\boldsymbol{B_0}$ will align the net magnetization ($\boldsymbol{M}$) of the hydrogen nuclei with the direction of $\boldsymbol{B_0}$. Then, an RF pulse is sent at the Larmor frequency of hydrogen nuclei to excite the hydrogen nuclei. During excitation, the $\boldsymbol{M}$ vector moves away from the $\boldsymbol{B_0}$ direction. Subsequently, longitudinal relaxation (T1) and transverse relaxation (T2) occur, which result in a magnetic moment causing the spins to induce a changing magnetic flux in the receiver coils of the MRI. This signal is detected and used to form the MRI images [10]. For generating images with MRI, there is an inherent trade-off between spatial resolution, temporal resolution and signal-to-noise ratio (SNR). These factors must be balanced and can be achieved by numerous MRI sequences, each benefiting specific imaging goals.

2.2.1 MRI sequences

Image acquisition in MRI is performed via pulse sequences, which describe the control signals that drive the gradient and RF systems. MRI-sequences are made by varying the order and values of certain components and parameters such as the applied RF-pulses, applied gradients, echo time (TE) and repetition time (TR). The TE is the time equal to the center of the RF-pulse to the center of the echo. The TR is the time of the interval between the corresponding points in consecutive cycles of pulses and echoes. By varying these components and parameters, each sequence is designed to emphasize specific characteristics of the tissue. This thesis will focus on two specific MRI sequences, (spoiled) gradient recalled echo (GRE) and balanced steady-state free precession (bSSFP). These sequences offer a high temporal resolution enabling real-time MRI combined with sufficient spatial resolution and contrast for interventional devices.

2.2.2 Slice selection

Image formation in MRI is based on three independent steps: slice selection, phase encoding and frequency encoding. During slice selection, a linear magnetic field gradient is enabled and a specific RF-pulse ensures that only the hydrogen nuclei are excited within the chosen slice. As the gradient fields can be applied with any combination, slices can be selected at any arbitrary location and angle. Subsequently, phase and frequency encoding steps are applied within the slice to localize the signal and form the image.

2.3 iMRI

Unlike diagnostic MRI, iMRI is tailored to enable fast image acquisition, reconstruction and processing for clinical interventions. The current technological standard in terms of hardware and software enables imaging with a frame rate up to 5-15 frames per second, depending on the application [11, 12]. Commonly used sequences suitable for iMRI are spoiled GRE, single-shot fast spin echo (FSE) and bSSFP. For iMRI, a high temporal resolution has the highest priority, often at the expense of spatial resolution and SNR. Some vendors have also developed dedicated software interfaces that enable live adjustment of the acquisition settings, such as adjustments in the image acquisition plane.

For catheter guidance, GRE and bSSFP sequences are most commonly used [12, 13, 14]. GRE sequences have demonstrated to be more resistant to artifacts, whereas bSSFP sequences achieve higher SNR [12]. Additionally, bSSFP sequences offer a superior blood-myocardium contrast because of their T_2/T_1 contrast [11]. Beyond cardiac applications, the excellent blood-tissue contrast provided by bSSFP also makes it appealing for other endovascular procedures. This is also supported by the comparative study of Reinok et al., which states that bSSFP results in a higher contrast-to-noise ratio (CNR) and a better visualization of a guidewire compared to GRE in a static phantom [8].

2.4 Guidewire tracking

Endovascular guidewire tracking can be categorized into two main techniques: active or passive tracking. In active tracking, RF microcoils are embedded into a device and connected to the RF receiver of an MRI system to overlay of the coil positions with the image [6, 7]. This localization process is very fast and does not risk out-of-plane motion. The microcoil signal can also be used as an additional RF receive coil and combined with conventional imaging coils into a composite image, which results in a localized hyperintensity indicating the position of the device [15]. The imaging sequence can be interleaved with tracking modules to enable dynamic slice repositioning while visualizing the anatomy [16]. However, some drawbacks are the need for

an RF interface with the MRI scanner and the guidewires used for these active tracking procedures are often relatively thick (e.g., 9F), which may cause additional challenges. Passive tracking techniques use intrinsic material characteristics to localize devices or markers, like the MRLine guidewire from EPflex [17]. There are multiple passive tracking techniques with embedded markers, coatings or balloon catheters based on different mechanisms: negative contrast, positive contrast, non-proton multi-spectral contrast and direct current [17].

When comparing active and passive tracking, active tracking is generally faster and more robust at localizing markers which benefits the ultimate goal of real-time MR-guidance [6, 17]. However, a main concern of active tracking devices it that the devices involve RF cables that can produce RF heating in the patient [6, 7]. Passive tracking requires manual slice plane adjustments, which can cause delays and compromise the clinical workflow. Compared to active tracking, passive tracking devices are generally cheaper to produce and do not need additional hardware or software (except for direct current passive tracking). These factors make passive tracking devices more appealing and easier to implement in a clinical setting. Therefore, this study focuses on passive tracking of a guidewire with embedded paramagnetic markers.

2.5 MRLine guidewire

Guidewires support precise navigation of catheters inside the vasculature. In MRI, not all guidewires can be safely used. For fluoroscopy purposes, guidewires often contain conductive materials or frequent presence of ferromagnetic components to create contrast and visualize the guidewires. However, these conductive materials and ferromagnetic components can induce RF-heating and are therefore in most cases not compatible for MRI [18]. For this study, an MRI compatible guidewire (MRLine, EPflex, Dettingen an der Erms, Germany) is used [19], see figure 2.1. This guidewire has embedded paramagnetic markers, which induce characteristic susceptibility artifacts suitable for passive tracking.

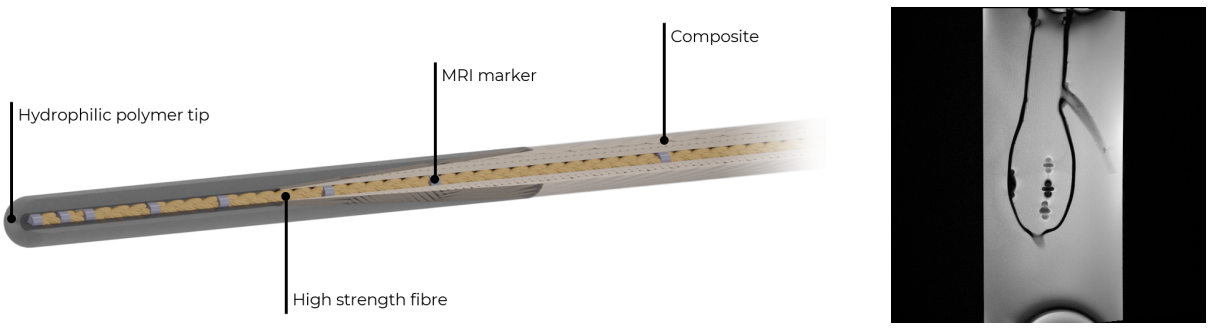

(a) The MRLine guidewire from [19]

(b) Appearance on MRI

Figure 2.1: A schematic visualization of the MRLine guidewire (left) and the MRI marker appearance on bSSFP images (right).

2.6 Marker detection

The passive markers of the guidewire result in susceptibility artifacts, presented as regions of signal loss as visualized in 2.1b. The markers must be accurately detected for performing interventional guidance procedures in the iMRI suite. Various detection approaches are explored, ranging from manual identification to more advanced techniques.

2.6.1 Manual

The conventional approach for passive marker detection is done by manual identification of the markers by an operator, which involves visual inspection of scanned MR images over time. While this approach is effective, it does have several limitations. The main limitation of this approach, is that this method is time consuming and therefore not suitable for real-time interventional applications. Furthermore, since the guidewire and its markers may move out of the scanned plane, it is difficult to determine their new position, which further complicates the tracking process. More efficient and accurate detection methods must be developed to improve the feasibility of iMRI for endovascular interventions.

2.6.2 White marker

As the susceptibility artifacts are regions of signal loss, simple thresholding techniques fail to provide accurate marker detection. A new method, potentially suitable for thresholding techniques, is white marker tracking. White marker tracking applies an MRI sequence which will give the susceptibility artifacts a positive contrast to its background. This is based on introducing additional gradients that dephase the background signal, while the signal surrounding the dipole susceptibility artifact is (partially) conserved [20, 21]. The white marker phenomenon is shown in figure 2.2. An advantage of this white marker phenomenon is that it increases the contrast and size of the marker signal [21]. However, this method does require specialized sequences which do not produce an anatomical image for navigation.

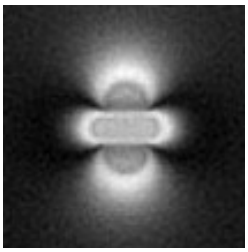

Figure 2.2: The white marker effect of the susceptibility artifact from [20]

2.6.3 Deep learning

An innovative approach that is able to maintain the anatomical image is for navigation is utilizing artificial intelligence (AI)-based methods like deep learning. Deep learning is an emerging technology for processing large amounts of data for medical applications, such as image classification, segmentation, reconstruction and detection [22, 23]. These networks need to be trained with a lot of data, often combined with specific generalization and regularization techniques to enhance the performance and prevent overfitting of the network [24]. In particular, convolutional neural network (CNN)'s have proven to be successful for segmentation, classification and detection tasks with a high accuracy on MRI scans [25, 26], making CNN's suitable for the detection of susceptibility artifacts induced by the embedded markers of the guidewire.

A phantom study performed by Reinok et al. showed a successful CNN for automated passive tracking of a guidewire with embedded paramagnetic markers [8]. A CNN was trained to automatically detect the susceptibility artifacts induced by the markers. However, this network is solely trained to detect markers whose coronal cross sections are perfectly aligned on the scan slice. This thesis aims to extent this approach and include markers with different orientations and positions, as such variations can provide essential input for slice realignment procedures. This would not only increase the robustness of the model and its detection accuracy, but would allow extracting additional information to facilitate automated passive tracking.

3 Research Approach

For the development of an enhanced and automated guidewire tracking system for iMRI, a structured research project has been conducted. The main research question that this thesis will cover is:

> *'How can an iMRI-guidance system be established to automatically track and navigate guidewires with embedded paramagnetic markers through a three-dimensional geometry with a high temporal resolution?'*

This research question will be approached through three core objectives.

3.1 Research objectives

The ultimate goal is to provide an iMRI guidewire tracking system that could be incorporated into clinical workflows. This thesis will focus on some key aspects that are crucial before implementing such a tracking system. Three core objectives form a general guideline and follow the order in which they will be executed. Each objective addresses a specific technical challenge and represents a different stage of this thesis. Together, they form the proposed solution for an automatic 3D tracking system for MR-guided interventions, see figure 3.1.

1. *Develop a passive marker simulation accurately representing any orientation and position.*
2. *Develop an automated marker detection software tool with the ability to detect arbitrarily oriented and positioned passive markers.*
3. *Develop a slice repositioning algorithm for 3D automated passive marker tracking during guidewire movement.*

3.1.1 Passive marker simulation

The initial phase of this thesis will focus on developing a passive marker simulation capable of accurately representing any orientation and position. Building on the work of Reinok et al. [8], this simulation will become an extension of its existing framework, enhancing its adaptability and precision. The optimized passive marker simulation will serve as input for the subsequent phase of this thesis.

3.1.2 Automated marker detection

The second phase of this thesis will involve the development of an AI-based procedure that is able to automatically detect the passive markers of the guidewire. Due to inherent movements of the guidewire and slice angulation during guided procedures, the model must be robust to variations in marker appearance.

To achieve such a procedure, aCNN will be trained with the extended passive marker simulation from the previous phase, to recognize these different appearances of the markers.

For training, a dataset must be build that represents different appearances of markers in a relevant environment. An endovascular phantom of an AAA will be used as a relevant environment. An efficient approach is chosen where passive marker simulations are artificially integrated into a training dataset, instead of capturing a significant amount of MRI data of the markers. A previous study by Reinok et al. has already shown the potential of this concept [8]. The output of the trained network will be used as input variables for an automated slice repositioning algorithm that will be developed in the last phase of this thesis.

3.1.3 Automated slice repositioning

Once the marker detection model can detect passive markers while having different orientations and positions, this objective will focus on developing an automated slice repositioning algorithm. This algorithm must be able to follow markers across multiple MRI slices and automatically shift position and/or orientation of the imaging plane.

The algorithm will be tested and evaluated on experimental MRI data with simulated marker movements. A simulation is build for systematic evaluation of the automated tracking algorithm and it enables easy testing different settings. It is important that the guidewire can be dynamically tracked within the phantom and that the computational time needed for the automated slice repositioning algorithm does not limit the temporal resolution of the iMRI system. During testing, the algorithm will be further optimized and refined to enhance the performance of guidewire tracking through a 3D geometry.

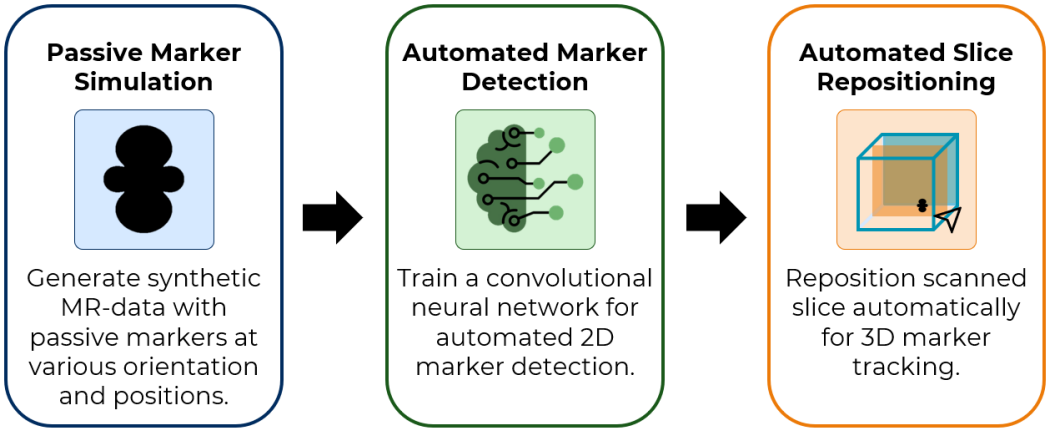

Figure 3.1: A graphic of the proposed solution to establish an iMRI system for automatic 3D tracking of guidewires with embedded passive markers.

4 | Passive Marker Simulation

This chapter describes the principle and the effect of susceptibility artifacts induced by passive markers on MR images. It will also outline the method that is developed to simulate these artifacts and validate the simulations with experimental MR data. All MR data was acquired on a 1.5T MRI system (MAGNETOM Aera, Siemens Healthineers, Erlangen, Germany) and the MRLine guidewire and a phantom of an AAA were used for the experiments, shown in figure 4.1.

(a) (b)

Figure 4.1: The (a) 1.5T MRI system and (b) abdominal aortic aneurysm phantom.

4.1 Susceptibility artifacts

Magnetic susceptibility (χ) is an intrinsic material characteristic quantifying a material's response to an applied magnetic field [27, 28]. A localized magnetic susceptibility can disperse the main field (=diamagnetic) or concentrate the main field (=(super)para- or ferromagnetic), inducing local inhomogeneities in the static magnetic field $\boldsymbol{B_0}$. These local inhomogeneities lead to localized image artifacts, with different sequences showing different sensitivities.

The guidewire that is used in this thesis uses passive susceptibility markers to enable visualization of the guidewire on an MRI image. As the guidewire contains embedded paramagnetic markers, the markers cause a 3D local field distortion with a defined symmetric shape which is shown in figure 4.2. As the inhomogeneity extends beyond the guidewire itself, and distorts the magnetic field in the surrounding lumen, the guidewire will be recognizable on an MRI image.

4.2 Simulation of susceptibility artifacts

As the markers cause a 3D local field distortion with a defined shape, it was attempted to simulate its shape in Python. With this simulation synthetic data was generated to train CNN's, to reduce the reliance on scanning multiple patients and accelerate the development of the automated 3D tracking algorithm. It is important that the simulation is representative of different marker orientations and positions within slices to enhance the robustness of the CNN's.

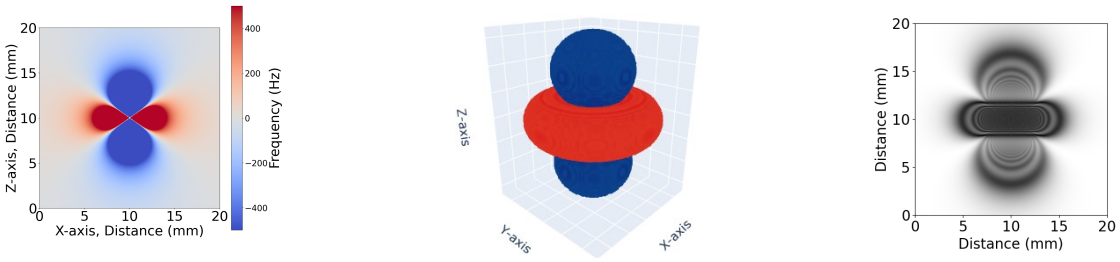

(a) (b) (c)

Figure 4.2: Visualization of the magnetic field distortion and susceptibility artifact. (a) A 2D visualization of the magnetic field distortion, (b) a 3D visualization of the defined shape of the field distortion and (c) a simulation of the resulting susceptibility artifact.

4.2.1 The effect on the local magnetic field

The passive markers of the guidewire are small paramagnetic rings creating field inhomogeneities as described in section 4.1. The markers cause signal loss and the averaged voxel signal can be mathematically described for gradient-echo sequences as a magnetic dipole with the following formula (4.1) [20]:

$$B_z = \frac{B_0 \cdot \Delta\chi V}{4\pi} \cdot \frac{(x^2 + y^2 - 2z^2)}{(x^2 + y^2 + z^2)^{\frac{5}{2}}} \tag{4.1}$$

Here, B_0 is the static magnetic field aligned along the z-axis, $\Delta\chi$ is the magnetic susceptibility difference between the marker material and the surrounding tissue, V is the volume of the paramagnetic material, and x, y, and z correspond to the spatial coordinates.

As the signal is integrated over the thickness of the slice (see equation 4.2), the artifact becomes visible in the scan due to dephasing.

$$S = \int_{-d/2}^{d/2} \rho(x,y,z) \exp(-i\gamma B_z \,\mathrm{TE})\, dz \tag{4.2}$$

Where $p(x,y,z)$ is the spin density in the x, y and z directions, d is the slice thickness in mm, γ is the gyromagnetic ratio of the hydrogen nuclei in Hz/T and TE represents the echo time.

With the use of these equations, the artifact can be simulated and also recognized in a scan of the guidewire.

4.2.2 Susceptibility artifact translation

During a catheter guidance procedure, the passive marker appearance will change over time due to translation as a result of guidewire movement and slice repositioning. For example, when a marker moves out of the scanned plane, the marker appearance changes, see figure 4.3. Eventually, the to be developed neural network has to be able to detect passive markers regardless of its position within the scanned slice. Besides translation of the marker, slice thickness also affects the appearance of the passive markers. Within this thesis all images are made with a slice thickness set at 5 mm.

To simulate the effects of translation and slice thickness on the susceptibility artifacts, a code has been written that selects simulation data based on a selected position and interval. Here, the position of the marker relative to the center of the scanned slice is called the *offset* and the interval represents the slice thickness. For the comparison between the simulated and scanned passive markers that will be made in section 4.3, three marker offsets due to translation are selected. These offsets are called *center*, *intermediate* and *adjacent*. Since scans will be made with a slice thickness of 5 mm within this thesis, an interval of 5 mm has been selected to maintain consistency with the scanning resolution. The simulation data inside the yellow regions representing the scanned slice from figure 4.3, will be integrated according to equation 4.2.

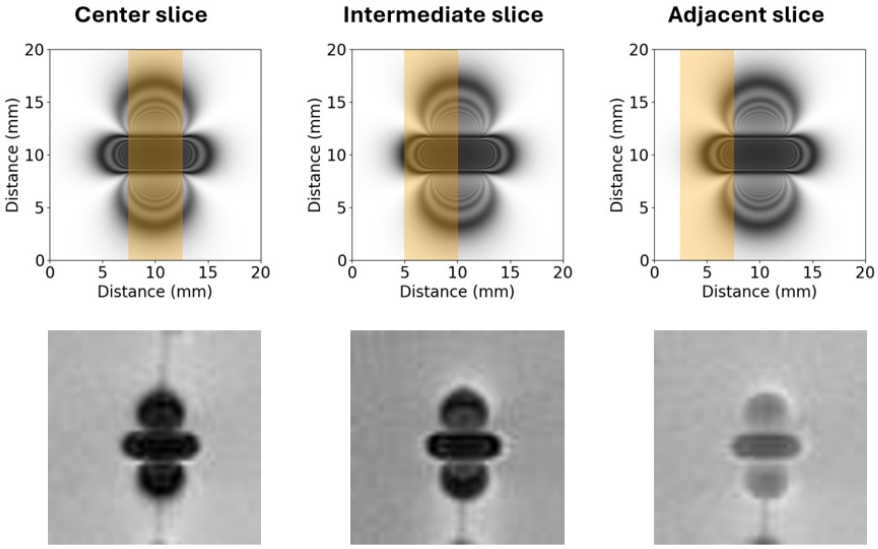

Figure 4.3: A visualization of different susceptibility artifact appearances as a result of translation.

4.2.3 Slice rotation

To maximally exploit the degrees of freedom in MRI to image under any plane, it would be beneficial to account for slice angulation in the modeling process. If the scanned slice has an angle with the z-axis, marker appearance changes due to rotation. An example of the rotation effect is visualized in figure 4.4. Detection strategies will also need to be able to detect the susceptibility artifacts regardless of angulation of the imaging plane. Therefore, the model has been extended to include effects of slice angulation on the marker appearance.

The implementation is based on Rodrigues' rotation formula, which is an algorithm that performs 3D rotation of a volumetric dataset around a specified axes [29]. Note that the code rotates the off-resonance data around its center rather than rotating the image plane, which is consistent with the sampling grid of the rotated image. This approach simplifies the code while preserving the intended effect of rotation on the passive marker appearances. A visualization of this approach is shown for two angles 30° and 90° in figure 4.5.

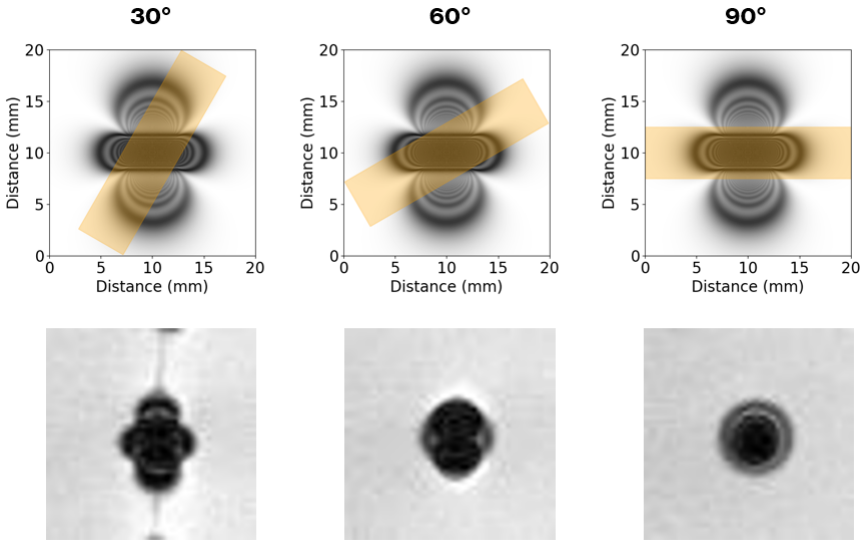

Figure 4.4: A visualization of different susceptibility artifact appearances as a result of slice rotation.

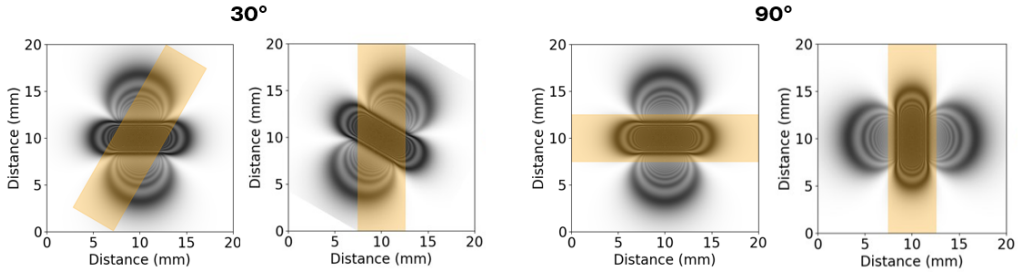

Figure 4.5: The rotation strategy used for the susceptibility artifact simulation where the entire simulation volume rotates (right images per angle) compared to slice rotation (left images per angle).

Given a specified axis of rotation $\mathbf{a} = [a_x, a_y, a_z]$ and a rotation angle θ, the rotation matrix $rot_{3d}(mat)$ is constructed as follows. First, the skew-symmetric cross-product matrix $\mathbf{W}$ is defined as:

$$\mathbf{W} = \begin{bmatrix} 0 & -a_z & a_y \\ a_z & 0 & -a_x \\ -a_y & a_x & 0 \end{bmatrix}$$

With the use of this matrix, Rodrigues' rotation matrix is written as:

$$\mathbf{R} = \mathbf{I} + \mathbf{W}\sin(\theta) + \mathbf{W}^2(1 - \cos(\theta))$$

Where $\mathbf{I}$ is the 3×3 identity matrix.

This rotation matrix is applied to the off-resonance data after shifting the coordinate system to the center of the volume to ensure that the volumetric data rotates around its center. The *RegularGridInterpolator* function from the *SciPy* package is then used to interpolate the rotated data points onto the original coordinate grid.

4.2.4 Experiment

Susceptibility artifacts with different slice offsets, a fixed slice thickness of 5 mm, a high resolution of 0.5x0.5 mm and various rotations of 0°, 30°, 60° and 90° are simulated and compared to susceptibility artifacts scanned with a spoiled GRE or bSSFP sequence. The respective scan parameters were: for the spoiled GRE sequence,

TR/TE = 9.6/5.0 ms, FA = 10°, field of view (FOV) = 384×384 mm, voxel size = 0.75×0.75 mm, slice thickness = 5 mm; for the bSSFP sequence, TR/TE = 4/2 ms, FA = 50°, GRAPPA = 2, FOV = 256×256 mm, voxel size = 0.75×0.75 mm, slice thickness = 5 mm, TA = 400 ms.

4.3 Results

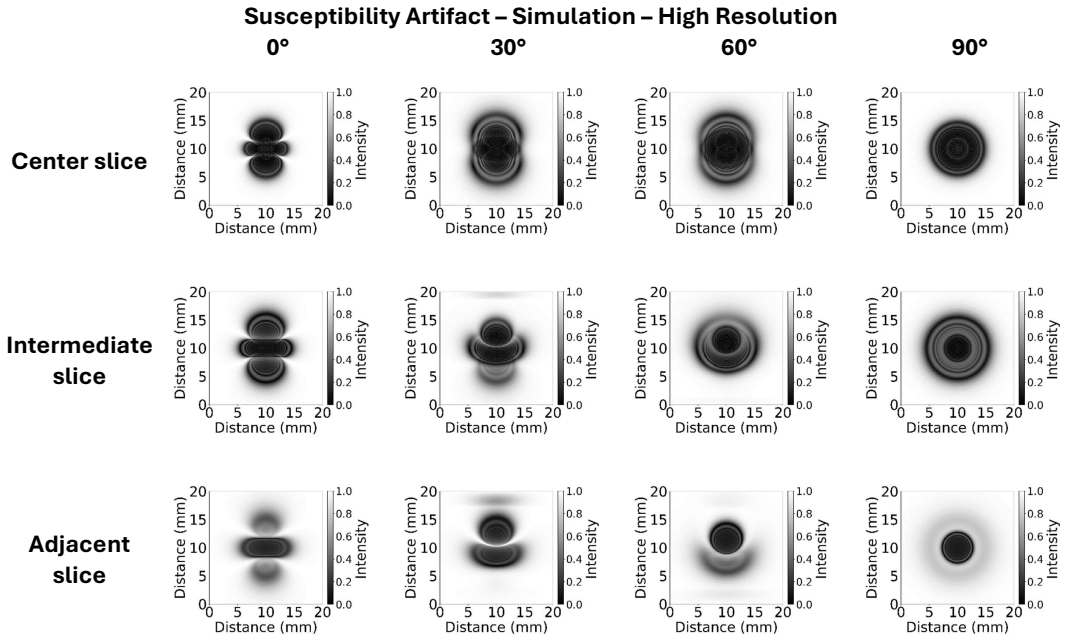

Figure 4.6: The simulated susceptibility artifacts caused by paramagnetic markers of the centered, intermediate and adjacent slice positions under the angles (from left to right): 0°, 30°, 60° and 90°.

The results of the simulated marker appearance for all angles and slice positions are visualized in figure 4.6. The marker appearances of real MRI images with a high resolution are shown in figures 4.7 and 4.8. Since bSSFP will be used for the rest of this research, a low resolution (1.6×1.6 mm) comparison between simulated artifacts and bSSFP scanned artifacts are shown in figures 4.9 and 4.10.

The comparison between the simulated susceptibility artifacts and the susceptibility artifacts acquired with bSSFP and spoiled GRE sequences demonstrated a strong agreement in artifact appearance. The simulated artifacts accurately reflect the general shape, size and intensities for different angles and slice position of the scanned images from both sequences. Despite some minor variations in intensity, particularly in adjacent bSSFP slices, the overall shape of the susceptibility artifacts was found to be similar between the high- and low-resolution simulated artifacts and the scanned artifacts.

A variation in the intensity of the artifact was observed when comparing artifacts from adjacent slices of the bSSFP images. The cause of this intensity variation remains unclear, but it is suggested that additional factors, such as sequence-dependent signal variations that are not included in the simulation, may influence the artifact appearance on bSSFP scanned images.

Furthermore, it was observed that the size of the susceptibility artifacts appeared larger on the images scanned with bSSFP compared to the images scanned with spoiled GRE, see figure 4.11. The difference in size was

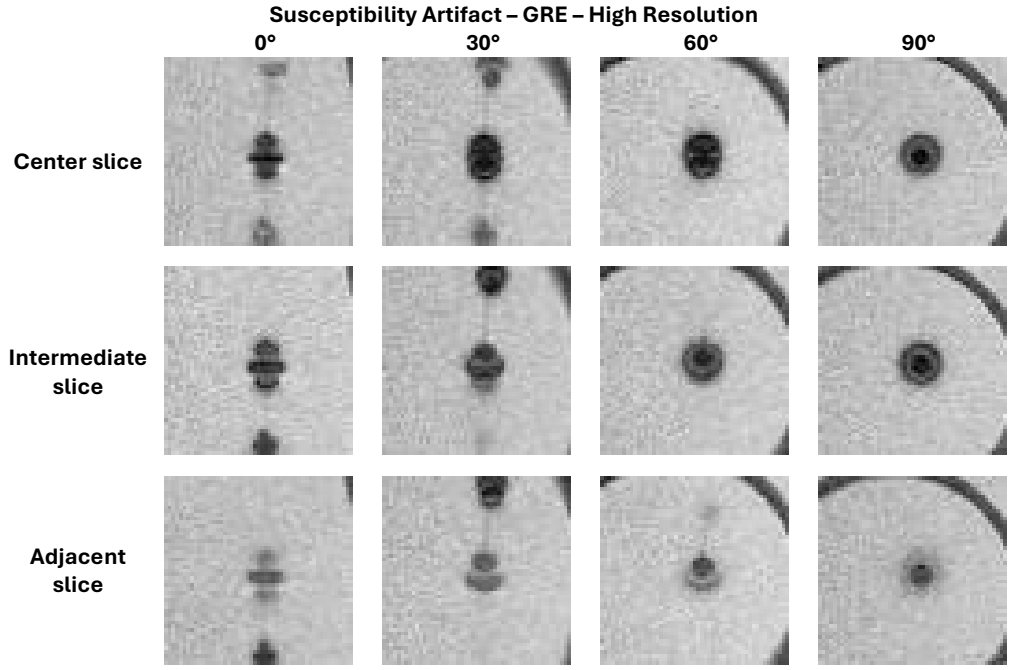

Figure 4.7: The susceptibility artifacts caused by paramagnetic markers scanned with GRE with a high resolution (0.5x0.5mm) of the centered, intermediate and adjacent slice positions under the angles (from left to right): 0°, 30°, 60° and 90°.

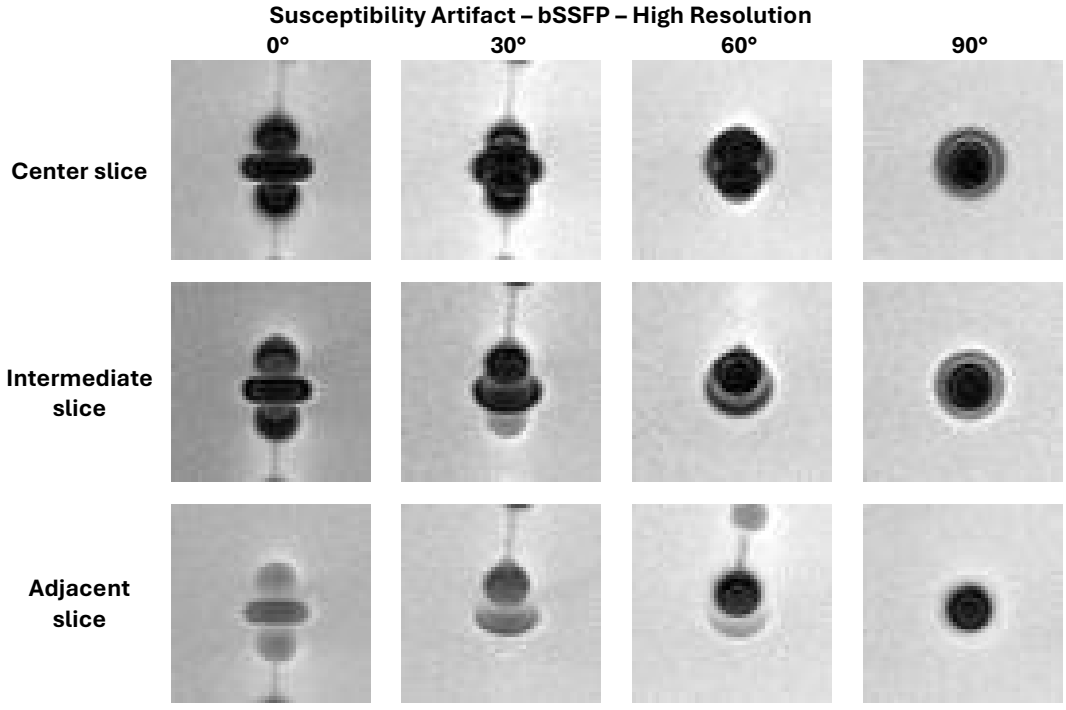

Figure 4.8: The susceptibility artifacts caused by paramagnetic markers scanned with bSSFP with a high resolution (0.5x0.5mm) of the centered, intermediate and adjacent slice positions under the angles (from left to right): 0°, 30°, 60° and 90°.

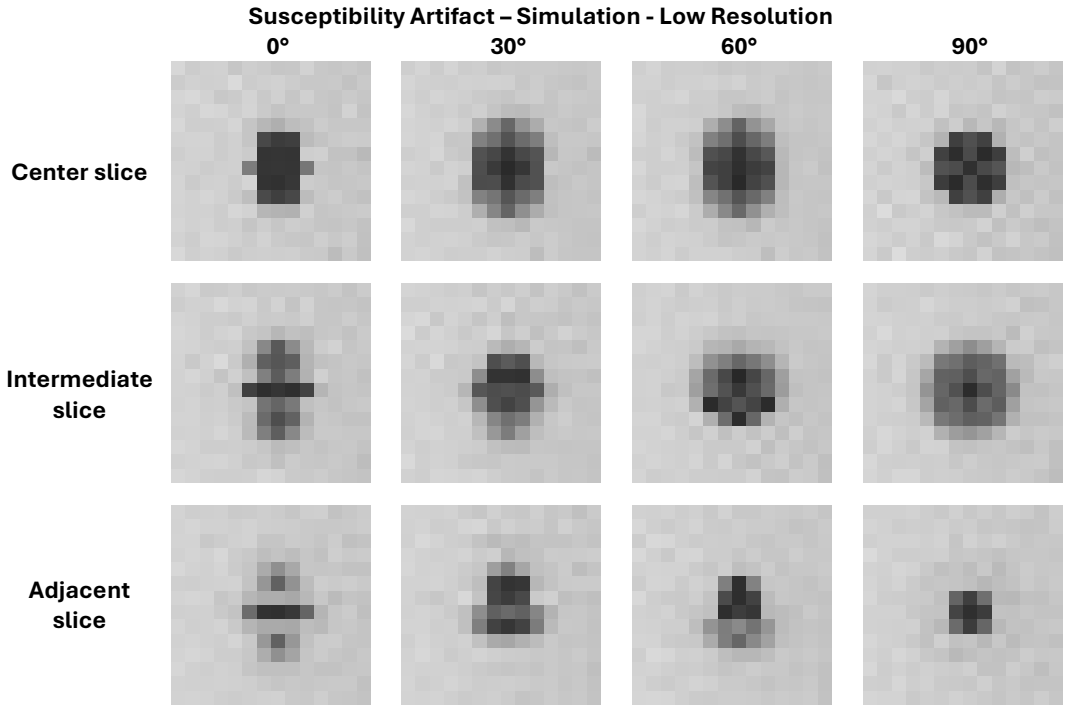

Figure 4.9: The simulated susceptibility artifacts caused by paramagnetic markers with a low resolution of the centered, intermediate and adjacent slice positions under the angles (from left to right): 0°, 30°, 60° and 90°.

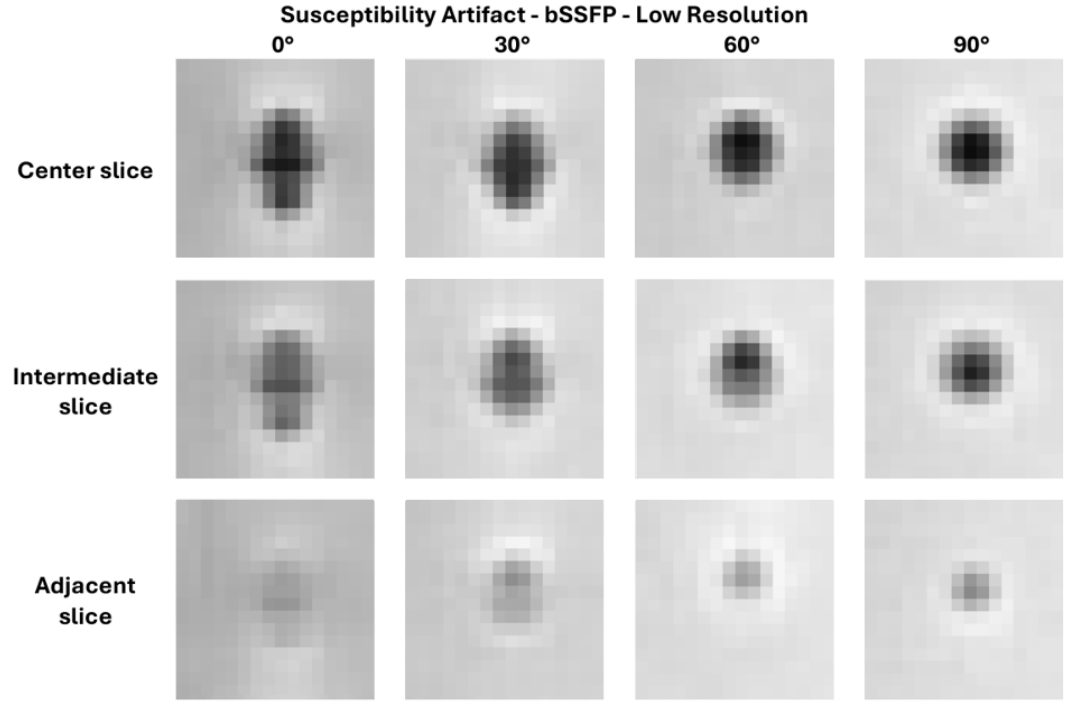

Figure 4.10: The susceptibility artifacts caused by paramagnetic markers scanned with bSSFP with a low resolution (1.6×1.6mm) of the centered, intermediate and adjacent slice positions under the angles (from left to right): 0°, 30°, 60° and 90°.

solved by increasing a scale factor for the dipole strength to obtain the correct marker appearance for both sequences.

(a) bSSFP (b) spoiled GRE

Figure 4.11: A comparison between the lengths of the bSSFP and spoiled GRE scanned susceptibility artifacts.

During scanning of markers with a high resolution bSSFP sequence, $\boldsymbol{B_0}$ shimming was found to have a great influence on the shape of the passive marker artifacts. Shimming is commonly applied to reduce banding artifacts caused by field inhomogeneities. It was seen that without shimming, banding artifacts were present around the markers changing the appearance of the artifacts. A visualization of the banding artifacts caused by markers is given in figure 4.12. Therefore, shimming is applied when scanning with bSSFP.

(a) 0°, center slice (b) 30°, intermediate slice

Figure 4.12: A comparison between the bSSFP scanned susceptibility artifacts with and without shimming applied. The first image shows the scan with shimming, the second without shimming and the third is an overlay to highlight the differences.

4.4 Conclusion

The results demonstrate that the simulations of the artifacts match the appearances of scanned artifacts in both GRE and bSSFP sequences. It therefore confirms the validity of the marker simulation, which will be further used for this thesis.

5 Automated Marker Detection

To be able to automatically follow and guide a guidewire during an endovascular procedure, the passive markers of the guidewire must be accurately detected and located, regardless the orientation and position of the markers and the scanned slice. The detection step will be performed by using deep learning, as CNN's have proven to be successful for classification and detection tasks with a high accuracy [25, 26], as discussed in section 2.6. This makes CNN's suitable for the detection of susceptibility artifacts induced by embedded passive markers of a guidewire.

This chapter explores the detection performance of two CNN's: the nnUNet of F. Isensee et al. and a customized CNN using a heatmap approach [30]. First, an overview of the dataset preparation process is given. Then, a description is given of the models and its evaluation metrics after which a comparison is made between the detection performance of both networks. Finally, the added value of training a network with and without different marker appearances is also evaluated at the end of this chapter.

5.1 Synthetic dataset procedure

A large labeled dataset for training purposes was synthetically generated using Python. Simulated marker models were superimposed to experimental MRI data acquired of the phantom without a guidewire present, at random positions within the phantom and covering a wide range of geometric parameters such as slice offset and orientation. The pipeline of this procedure is visualized with a flowchart in figure 5.1.

The training data consists of 384 MR-slices with a resolution of 160×160 pixels, containing 12 variations of the passive marker appearance as described in chapter 4. Both networks are trained with the same training data with corresponding labels. Here, the nnUNet utilizes a segmentation mask as a label and the the custom CNN utilizes a heatmap which involves a 3D Gaussian distribution originating a the center of the passive marker. A visualization of corresponding labels for a superimposed MR-slice is given in figure 5.2.

Diverse training data is needed for training a robust CNN, as it will improve model generalization [24]. By including variations in the passive marker appearance, marker size, amount of markers per image, random placement of markers and diverse background images, the train dataset contains a wide range of possible inputs. This is expected to improve the model's performance when new data is used as an input.

5.2 Network architectures

5.2.1 nnUNet

The nnUNet architecture from F. Isensee et al. is used for the detection of guidewire markers [30]. The nnUNet is known for its ability to segment structures within images, which can be extended to determine the position

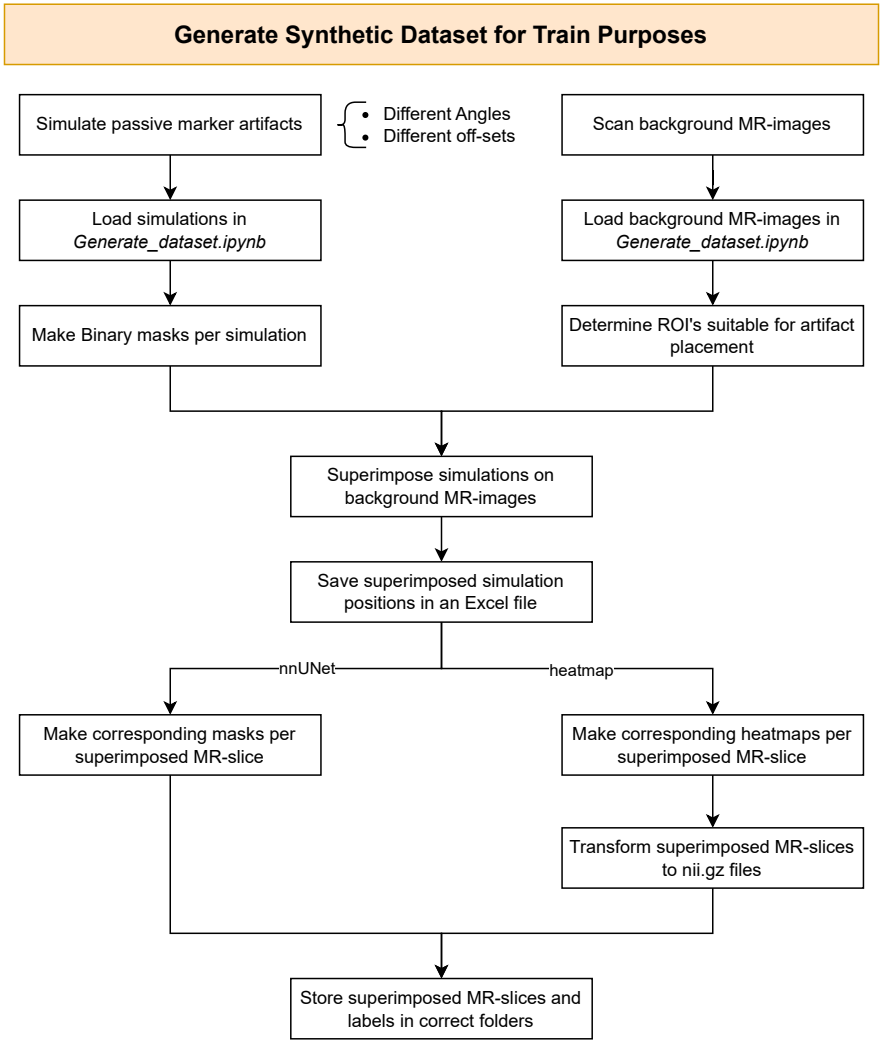

Figure 5.1: Detailed description of the methodology for generating a synthetic dataset for training purposes, visualized using a flowchart

of such a segmented structure. This approach enables the detection of passive markers and contributes to the goal of passive marker tracking.

First, the nnUNet determines a so called "data fingerprint" of the train dataset, containing hyper-parameters like loss function, optimizer, architecture of the model, image resampling, image normalization etc. These hyper-parameters are automatically specific and optimized per train dataset by the nnUNet. Then the network follows a U-shaped convolutional architecture, and is suitable for 2D, 3D and 3DC datasets. For this thesis, the 2D architecture is utilized. The models' architecture contains 6 stages, uses Dice Loss as loss function and LeakyReLu as activation function. Before training, the dataset is split into 5 folds to perform k-fold cross-validation. Eventually, all folds are ensembled to form the final network. Predictions are based on taking the argmax of the combined softmax probability maps from all 5 folds.

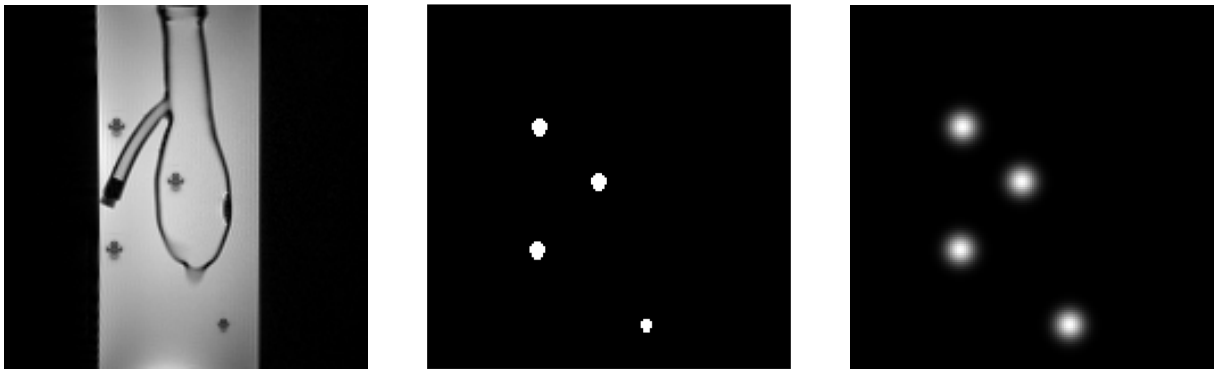

(a) Synthetic image data with four marker artifacts.

(b) Corresponding segmentation label for nnUNet

(c) Corresponding heatmap label for custom heatmap CNN

Figure 5.2: An example of the image pairs in the training dataset.

5.2.2 Heatmap detection

The custom made heatmap detection CNN is made to detect passive markers by highlighting their locations on a heatmap. Unlike nnUNet, this model does not automatically optimize hyperparameters. However, it has the potential to distinguish markers by varying the intensities of generated hotspots. Therefore, this model is built to evaluate the capability of heatmap detection to detect and to differentiate markers that are present in center slices from those in adjacent slices.

The heatmap detection network follows a 2D U-net made with the *MONAI* package in Python [31]. The model contains 5 stages, utilizes ReLu as loss function and MSE Loss as loss function. 5-fold cross-validation was also performed.

5.3 Network comparison and evaluation

For the evaluation of the two networks, a test dataset was made. The test dataset contains 51 MR-images of the phantom with the marker-embedded guidewire inside, as the interested lies in the performance of the networks on real experimental MR-data. The MR-images were obtained with the TRUFI sequence of Siemens, which is a sequence that has a high temporal resolution and utilizes bSSFP. During scanning, the guidewire was moved to different positions in the phantom and scan planes were manually adjusted to obtain different MR-images. At a rate of approximately 3 scans per second, 5 slices were imaged at a time. Each subset of slices included an adjacent slice, an intermediate, the center slice, followed by the other intermediate and adjacent slices. The set up on the MRI-system is shown in figure 5.3. After obtaining the data, MR-images that included markers were manually selected resulting in a dataset of 51 MR-images for testing the networks. A comprehensive overview of the train, validation and test datasets is visualized in figure 5.4.

Both networks were tested on the test dataset and their predictions were manually assessed. An example of their predictions is given in figure 5.5. The evaluation of the two networks revealed a strong difference in their detection performance. The heatmap detection network performed poorly in detecting markers and generated numerous false positives, making it an unreliable network for marker detection. In comparison, the nnUNet outperformed the heatmap detection network, as it identified most markers correctly with fewer false positives. Therefore, the nnUNet will be further used for this thesis.

Figure 5.3: The experimental set-up for real-time scanning with TRUFI sequence for obtaining the test dataset

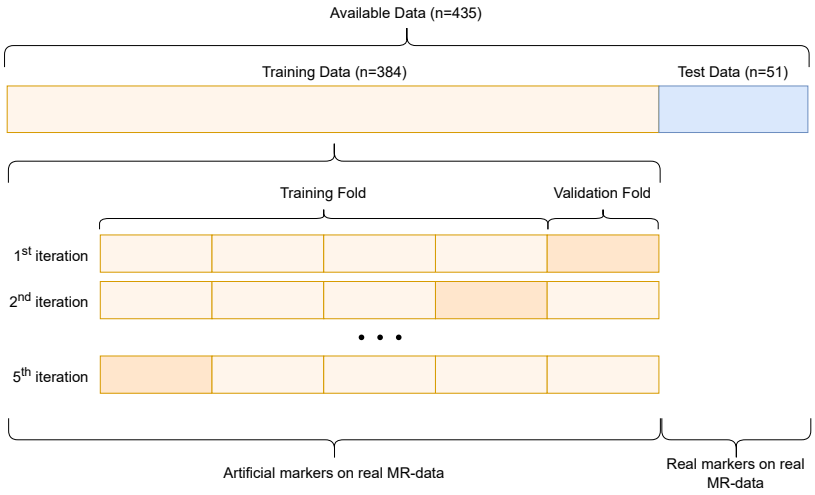

Figure 5.4: A comprehensive overview of the train, validation and test dataset for the trained networks.

5.4 Influence of training data on performance

Section 4 already discussed the possibility of different marker appearances while imaging the guidewire. To evaluate the influence of training the model with these different marker appearances, nnUNet was trained with two different train datasets. One train dataset contains 384 superimposed MR-slices with a resolution of 160×160 pixels, containing the 12 variations of the passive marker appearance as described in chapter 4 and the other train dataset contains 384 superimposed MR-slices of the same resolution, but only with the marker appearance at center position and a 0° angle. The nnUNet trained with different marker appearances is called *nnUNet1* and the network trained with one marker appearance is called *nnUNet2*.

5.4.1 Methodology

To assess the detection performance of both models, they were tested on the test dataset of 51 MR-images as described in section 5.3. After their predictions were generated, the result was manually assessed. This was done by computing the F1 score and by computing the Dice score for all predictions. After individual assessment, a comparison between both performances was made.

(a) An original scan of three markers.

(b) Corresponding prediction of the nnUNet.

(c) Corresponding prediction of the heatmap network

Figure 5.5: An example of the image pairs in the training dataset.

F1 score

The F1 score is a metric for the accuracy of a model and is calculated by equation 5.1 [32]. The true positives (TP), false positives (FP) and false negatives (FN), see definitions in table 5.1, where manually counted for both the predictions of both networks.

$$F1 = \frac{2TP}{2TP + FP + FN} \tag{5.1}$$

True positive	The marker was predicted by the CNN and present in the MR-slice.
False positive	The marker was predicted by the CNN, but not present in the MR-slice.
False negative	The marker was not predicted by the CNN, but present in the MR-slice.

Table 5.1: The definitions of assessment criteria

Dice score

The Dice-score is a metric for the similarity between the ground truth mask and the prediction mask made by a network [33]. To compute the Dice score, all original MR-slices were manually labeled using Python. An example of an annotated ground truth label is shown in figure 5.6. Then, the predictions and ground truth labels were compared according equation 5.2.

$$D = \frac{2|A \cap B|}{|A| + |B|} \tag{5.2}$$

Here, D is the Dice score, A is the area of the ground truth label and B is the area of the prediction.

5.4.2 Results

F1 score

The amount of the manually counted TP's, FP's and FN's for the models *nnUNet1* and *nnUNet2* are shown in table 5.2. The results indicate that *nnUNet1* performed better at detecting the markers than *nnUNet2*, as it detected the most TP's and the highest F1 score. The detected FN's primarly occured when markers had an offset or when markers were close near a boarder of the phantom vessel. The detected FP's were low for both models, with *nnUNet1* detecting 11 FP's and *nnUNet2* 8.

(a) An original scan with four markers. (b) The corresponding annotated ground truth.

Figure 5.6: An example of an annotated ground truth label.

	nnUNet1	**nnUNet2**
TP	182	152
FP	11	8
FN	22	52
F1 score	0.92	0.84

Table 5.2: The F1 score results for *nnUNet1* and *nnUNet2*.

Dice score

The Dice scores were automatically calculated for all 51 MR-slices using Python. The mean and median Dice scores for both models are presented in table 5.3. The results show that *nnUNet1* achieved a higher mean and median Dice score compared to *nnUNet2*. This therefore indicates that *nnUNet1* is better at predicting accurate segmentions of the markers.

	nnUNet1	**nnUNet2**
Mean Dice score	0.76	0.70
Median Dice score	0.77	0.72

Table 5.3: The mean and median of the calculated Dice scores for *nnUNet1* and *nnUNet2*.

5.4.3 Conclusion

From both the F1 scores and the Dice scores, it can be concluded that training nnUNet with different marker orientations improves the real-life detection performance of the model as both metrics are higher for *nnUNet1* than *nnUNet2*. In figure 5.7, an example is shown where *nnUNet1* can detect a marker that has an offsett and *nnUNet2* can not.

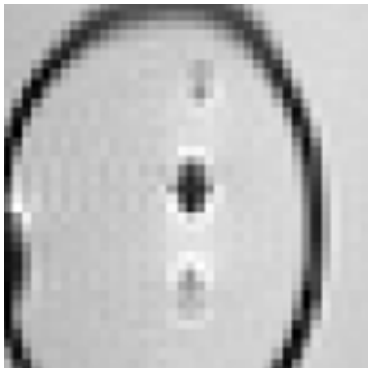

(a) An original scan of three markers.

(b) Corresponding prediction of *nnUNet1*.

(c) Corresponding prediction of *nnUNet2*.

Figure 5.7: The predictions of *nnUNet1* and *nnUNet2* for an experimental MR-image, where *nnUNet1* is capable of detecting markers with an offset and *nnUNet2* is not.

6 | Automated Marker Tracking

Solely using the predictions of the nnUNet for automated marker tracking could be done by scanning the entire 3D environment and analyze each slice. However, the acquisition time for the entire 3D environment does not meet the conditions for real-time scanning with iMRI. Therefore, a solution must be developed to track the passive markers with the condition of scanning the least amount of slices at a time to maximize the temporal resolution. The inherent risk of scanning fewer slices is that the markers could move out of the scanned slice(s) and are not detectable on the slice(s). All these aspects must be taken into consideration to develop an algorithm suited for clinical implementation.

In the current clinical workflow, marker tracking has to be done manually, which is time consuming and unintuitive. This chapter offers a promising solution for an intuitive and automated marker tracking algorithm while only scanning three slices at a time with a high temporal resolution of 1 second. First, the slice repositioning part is explained, after which a detailed description is given of the entire marker tracking algorithm. Subsequently, the intuitive visualization interface is shown and the algorithm is validated.

6.1 Slice repositioning

To track the passive markers in a direction perpendicular to the slice orientation, a slice repositioning algorithm is developed. The slice repositioning algorithm is based on a three-slice iteration. The algorithm processes three slices at a time to determine the x,y,z-position of the centroids of the markers and updates the slice index (= *XX*) for the new central slice position of the three slices. The three slices are obtained within one second ($\approx$ 0.8 sec) and are referenced as *XX*, *XX-1* and *XX+1*. These slices will be analyzed using the nnUNet model, which predicts the location of passive markers. From the predictions, the centroids of the markers are calculated and the weighted average of their z-positions determines the next target slice index for the central slice position. This process of updating the center slice position is integrated within a developed automated marker tracking algorithm and visualized in figure 6.1.

6.2 Marker tracking algorithm

The final marker tracking algorithm iterates the repositioning processing steps over time for each subset of three slices and ensures automated marker tracking for marker movement in all directions. The marker tracking algorithm is executed and tested in a closed-loop simulation programmed in Python. The simulation allows for testing different conditions in a controlled setting, minimizing experimental scan time and validating the algorithm before implementing the algorithm with iMRI. Before starting the tracking process, the algorithm requires the initial center slice position of a marker. In reality, this step can be achieved during a 'calibration' phase of the guidance procedure; i.e. identifying the marker within the full 3D geometry. The dataset used for

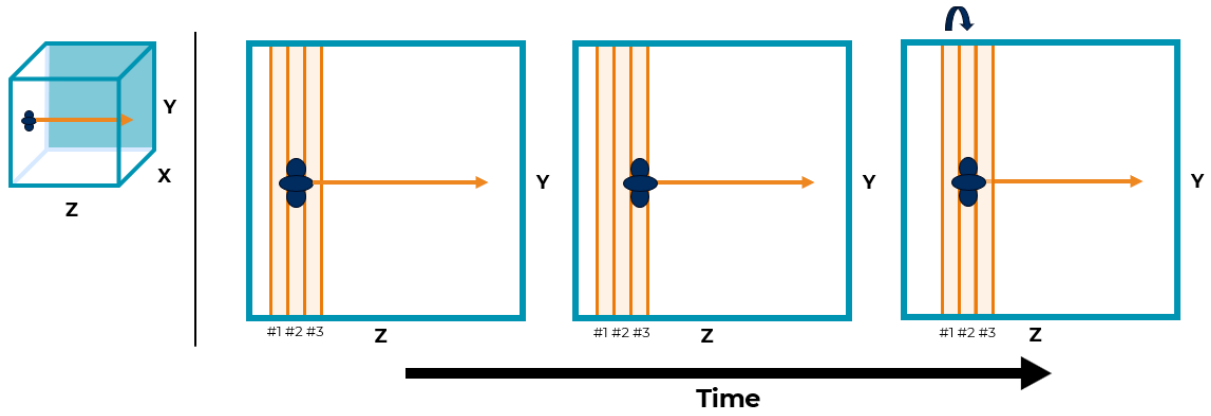

Figure 6.1: A schematic visualization of the slice repositioning algorithm updating the slice index due to marker movement.

the simulation contains time steps of 3D experimental MRI data, saved in separate time folders. Over time, marker movement is synthetically simulated in all 3D MRI data.

As the nnUNet is trained on grayscale (L-mode) png images with a resolution of 160×160 pixels and filename *susceptibility-generated_0XX_0000.png*, the three selected slices *XX-1*, *XX* and *XX+1* need to meet these requirements for its compatibility. Therefore, a pre-processing module is written that processes the three selected slices. If the image resolution differs from 160×160 pixels, the images are either cropped around the center, or zero-padded to 160×160 pixels. Once processed, the slices are analyzed by the nnUNet.

The predictions of the nnUNet are analyzed by the slice repositioning module. The individual predictions per slice are combined to 3D elements, where the algorithm distinguishes separate elements. Per detected element, the coordinates of the centroids are determined. For analyzing purposes, the centroids are determined and saved per timestep. The new center slice position *XX* is determined based on the weighted average of the z-position of all detected centroids. To minimize the effect of false positives given by the nnUNet, a threshold can be chosen to filter elements out that have an insufficient number of pixels. For this thesis, a threshold was set at 20 pixels, so detected elements with less than 20 pixels are neglected in this calculation. This decision making process, is visualized with an example of three subsequent iterations in Appendix A. This entire process is repeated through the sequence of time steps until the final time step is reached. A schematic presentation of the automated marker tracking algorithm in the closed-loop simulation is presented in figure 6.2.

6.3 Clinical implementation

An important aspect of the tracking algorithm is that it has to be compatible with the functionality of iMRI and intuitive for clinical implementation. As the TRUFI sequence of Siemens scans three parallel slices at a time per second, its interface shows the scanned slices and updates these once per second. With the implementation of the tracking algorithm, these slices are automatically processed after each acquisition in order to determine the marker positions.

For usability purposes of the automated tracking algorithm, an interface is designed that combines the visualization of the three scanned slices with the predictions of the nnUNet, supplemented with a 3D visualization of the marker and scanned slice positions within the scanned volume. This 3D visualization provides a broader perspective of the marker position in reference to the scanned volume and enables efficient monitoring of the tracking process. An example of the interface is given in figure 6.3.

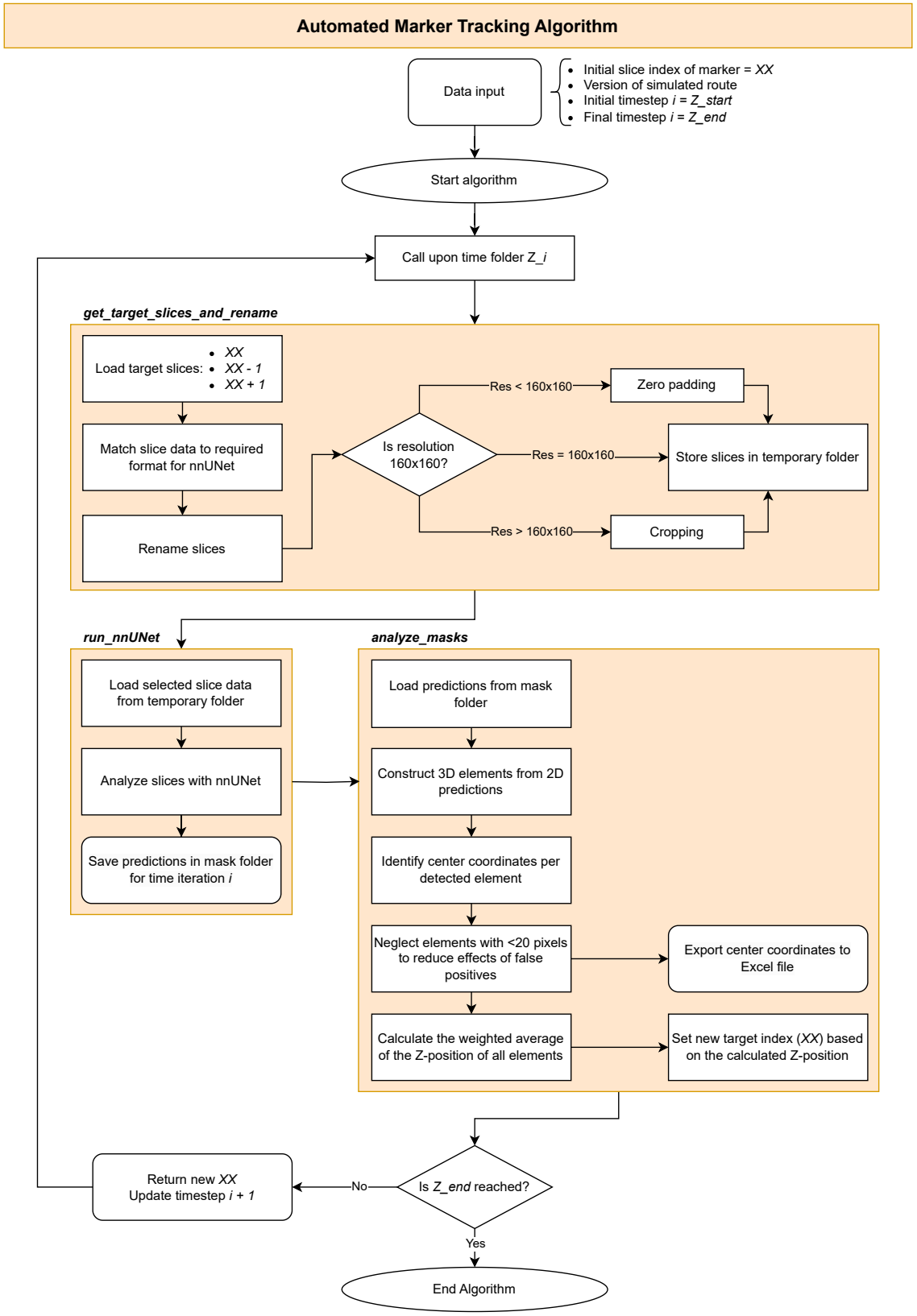

Figure 6.2: A detailed description of the methodology behind the developed automated marker tracking algorithm with marker detection by nnUNet and slice repositioning.

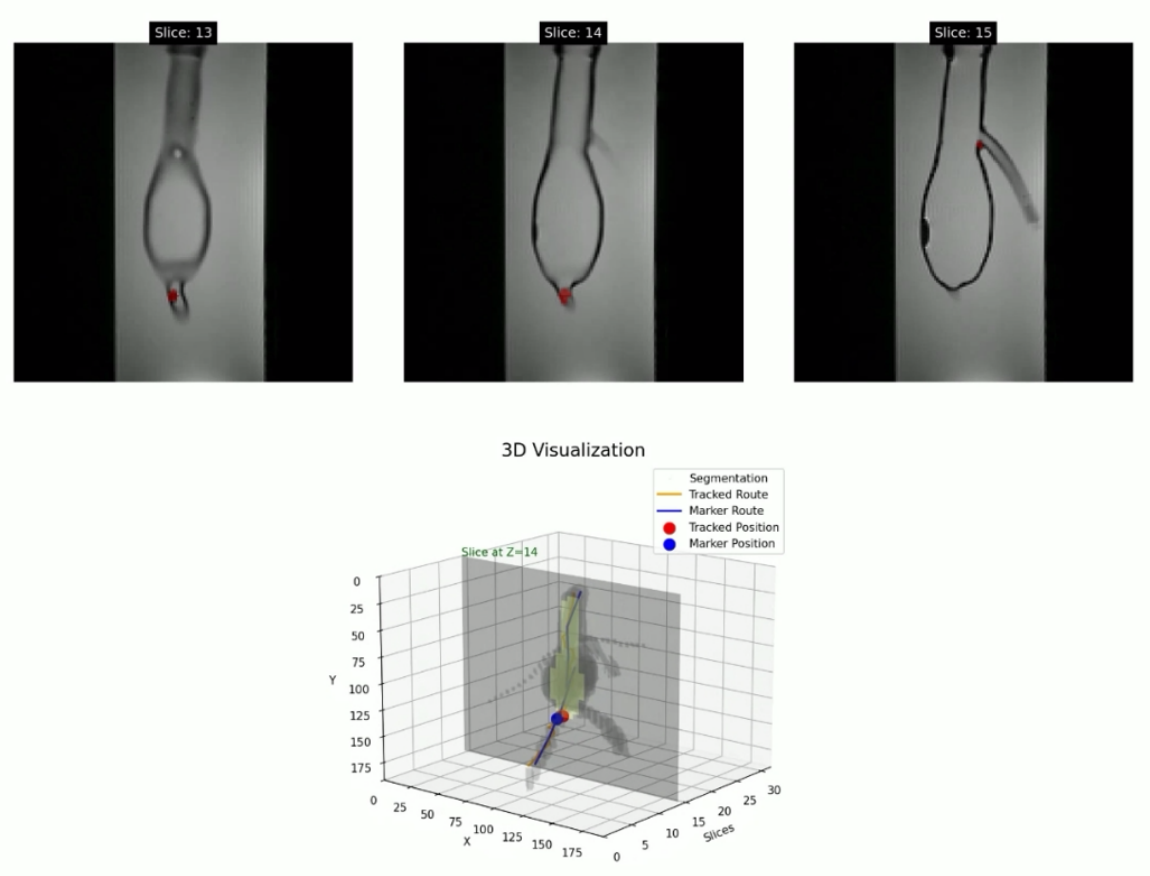

Figure 6.3: The interface of the tracking simulation demonstrating the automated marker tracking procedure. Above, the three scanned slices are visualized with the nnUNet assessment in red. Below, a 3D visualization is shown of the 3D space, where the blue dot represents the true marker location of its center and the red dot represents the predicted center of the marker. The position of center slice is also visualized as a reference to ensure spatial awareness.

6.4 Validation

The automated tracking algorithm is validated with dynamic experiments in the closed-loop simulation programmed in Python. A quantitative analysis is conducted for different motion patterns and for different marker velocities in the perpendicular direction of the slice orientation to analyze the performance of the automated tracking algorithm.

6.4.1 Methodology

To evaluate the ability of the automated marker tracking algorithm to track markers with different trajectories, four 3D synthetic datasets are constructed with a single marker moving along different trajectories. First, the tracking algorithm is tested on a marker moving in a straight path perpendicular to the slice orientation. Second, a marker moving along a diagonal path across the 3D geometry. Third, a marker making a back-and-forth movement and finally, a marker following a realistic trajectory through the AAA phantom, see figure 6.4.

In addition to testing different trajectories, the tracking performance is also evaluated at different marker velocities. The marker velocities are systematically increased with 0.5 mm/s to assess the performance under

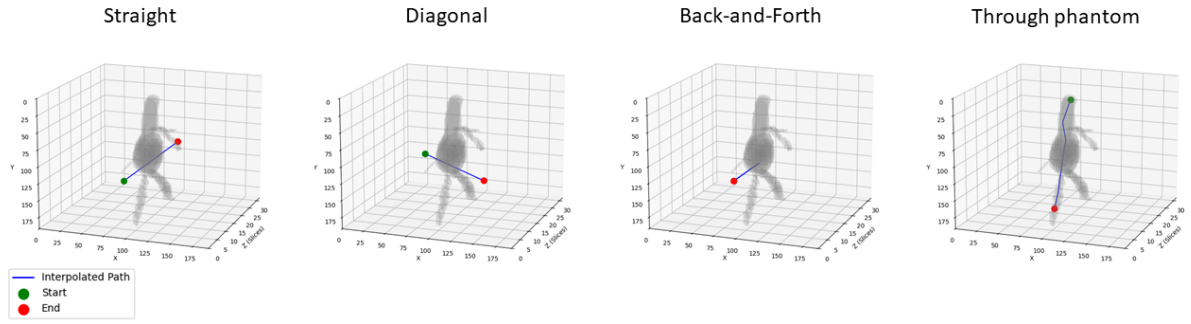

Figure 6.4: A visualization of the four tested trajectories relative to the 3D geometry.

different velocities and determine the speed limit of the moving marker. As marker movement in the direction perpendicular to the slice orientation is a critical bottleneck for tracking the marker, the markers follow a straight path along this direction.

To quantify the performance of the automated tracking algorithm, the root-mean-square error (RMSE) between the true and tracked marker positions is computed for each trajectory and velocity combination, see equation 6.1. In addition, the deviations per spatial dimension (x, y, and z) are assessed separately and the maximal euclidean distance is determined, providing a more detailed assessment of the accuracy.

$$\text{RMSE} = \sqrt{\frac{1}{n}\sum_{i=0}^{n}(p_i - \hat{p}_i)^2} \tag{6.1}$$

Where n is the amount of coordinates, p_i the true center coordinates of the marker position and $\hat{p}_i$ the determined center coordinates of the marker position by the tracking algorithm.

6.4.2 Results

The evaluation of the four different marker trajectories showed that the automated marker algorithm is capable of tracking all tested marker movements. For comparison, a fixed velocity of 4.0 mm/s was chosen. The results for each trajectory type are summarized in table 6.1 and the tracked marker routes compared to the original routes are plotted in Appendix B. Notably, the mean deviations in all directions and the maximal euclidean distance remain within one voxel size (1.6×1.6×5.0 mm), indicating a high tracking accuracy.

Trajectory	RMSE (mm)	Mean deviation in x-direction (mm)	Mean deviation in y-direction (mm)	Mean deviation in z-direction (mm)	Maximal Euclidean distance (mm)
Straight	3.5	0.0	0.5	3.2	5.4
Diagonal	2.3	0.6	0.7	1.6	4.2
Back-and-Forth	3.4	0.0	0.2	3.2	5.2
Through phantom	2.9	1.0	0.7	2.1	4.8

Table 6.1: Tracking performance results for different marker trajectories.

Table 6.2 shows the results for the five different velocities, ranging from 3.0 mm/s to 5.0 mm/s. The results indicate a trend where the accuracy decreases with higher velocities, see figure 6.5. The limit of the marker velocity was found to be 5.0 mm/s in the perpendicular direction of the slice orientation. No limit was found in the other two directions, as these are in plane movements and detected by the nnUNet. The mean deviation in the x-direction remains close to zero across all velocities, while the mean deviations in the y- and z-directions

fluctuate slightly. Here, it can also be observed that the mean deviations in each dimension remain within the corresponding size of one voxel, indicating a high tracking accuracy. A more detailed overview of the RMSE distribution and the deviation per dimension for all trajectories and velocities can be found in Appendix C and D.

Velocity (mm/s)	RMSE (mm)	Mean deviation in x-direction (mm)	Mean deviation in y-direction (mm)	Mean deviation in x-direction (mm)	Maximal euclidian distance (mm)
3.0	3.0	0.0	0.5	2.7	2.7
3.5	3.2	0.0	0.6	2.9	4.9
4.0	3.5	0.0	0.5	3.2	5.4
4.5	3.8	0.0	0.6	3.4	5.8
5.0	5.0	0.0	0.6	4.8	5.2

Table 6.2: Tracking performance results for different marker velocities.

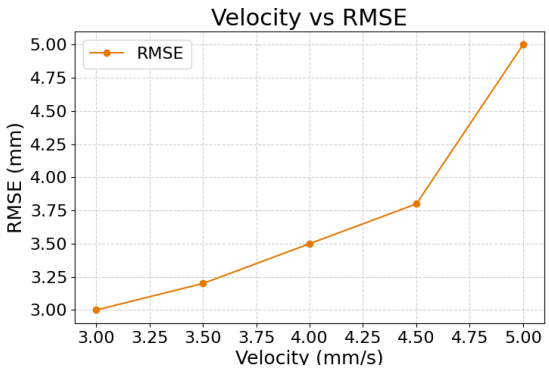

Figure 6.5: Tracking performance results at different marker velocities.

A remarkable observation in the validation of the tracking algorithm is that the nnUNet detects more pixels for slices adjacent to the marker, compared to the central slice. Specifically, the network consistently identifies 2 to 4 more pixels in the adjacent slices. This imbalance influences the selection of the slice index for the next iteration, as the calculation of the weighted average of centroid coordinates is biased toward the adjacent slice rather than the centered slice. As a result, the final marker tracking process could show a slight offset.

Overall, the automated marker tracking algorithm demonstrates robust performance across various marker movements and for different marker velocities, with a gradual decline in accuracy as the velocity increases.

6.5 Conclusion

By integrating nnUNet assessment and iterative slice repositioning, the marker tracking algorithm is able to extract the 3D position of markers and follow them as they move. The interface also provides an intuitive visualization of the 3D marker position in reference to patient-specific anatomy, making it a promising tool for comprehensive catheter guidance with iMRI.

7 Discussion

In this chapter, the findings of this thesis are discussed in relation to the performance of the detection network and the slice repositioning approach. Additionally, prospects for future research and potential improvements are presented to refine and expand upon the current work.

7.1 Detection network

Accurate marker detection is essential for effective tracking in interventional procedures. The nnUNet has proven to be successful for marker detection, demonstrating reliable performance across arbitrary marker orientations and positions. Training a network with a full range of slice orientations and off center positions improved the detection performance.

7.1.1 Detection performance nnUNet

It was observed that both *nnUNet1* and *nnUNet2* sometimes missed a marker or detected some false positives. All deviations were manually evaluated and clear causes were found. All false negatives can be attributed to the marker being not detected because its center was located in an adjacent slice or to the marker being positioned very close to the silicone border of the phantom. This silicone border of the phantom has a low intensity, just like the marker appearance, on MR images and small air bubbles can be present on the wall of the border. These bubbles create additional low-intensity regions, making it hard for the CNN's to distinguish actual markers from the background. Considering the false negatives due to the adjacent marker position, the slice repositioning algorithm scans three slices at a time. This multi-slice scanning reduces the reliance on a single off-center marker, making the detection process more robust in reality. The false positives can also all be attributed to the silicone border of the phantom as it was sometimes mistaken as a marker. However, these issues are unlikely to occur when scanning in vivo in a clinical setting instead of the phantom with a silicone border. A phantom without silicone or with a thinner wall would also reduce the presence of false positives. Furthermore, the presence of air bubbles, which contributed to false positives in the phantom, is not a concern in biological tissue. Therefore, it is expected that the CNN's will not make these errors when scanning markers in a clinical setting.

7.1.2 Limitations of the dice score

The Dice similarity coefficient was determined as a metric to evaluate the detection performance of both CNN's. Since both networks were assessed with the same annotated ground truth labels, a reliable and direct comparison could be made. However, the annotated labels were manually labeled in experimental data by a single individual. This introduces a potential bias, as variations in interpretation can affect the ground truth segmentation. Ideally, multiple annotators should be involved in the labeling process to reduce bias and

improve the reliability of the results. Despite this limitation, the results do provide a meaningful performance comparison of the CNN's. The F1-score complements this statement.

7.2 Automated marker tracking

The performance analysis of the automated marker tracking algorithm demonstrated promising results and can track a marker up to a speed of 5 mm/s in the perpendicular direction of the scanned slice, with a fixed slice thickness of 5 mm. The marker movement simulation gave valuable insights in the performance of the automated marker tracking algorithm.

7.2.1 Tracking delay

In the performance analysis of the slice repositioning algorithm, it was stated that the algorithm shows a slight delay between the actual movement of the marker and its detected position. This delay occurs for two main reasons. First, the algorithm processes the movement while the marker continues to move. Second, the algorithm determines the center of detection based on the contours of the predictions of the CNN, which can introduce further deviations. When a marker is detected in its adjacent slice, it is often detected with 2 to 4 more pixels than the center slice. This results in a small shift in the estimated center. As a result, the tracking lags behind the true position of the marker, especially in cases where the marker rapidly moves through different slices. Future improvements could focus on investigating the performance of the nnUNet for adjacent and center slice positions to enhance the automated tracking performance, as the size of its predictions are a cause of the slight delay.

7.2.2 Marker velocity

The automated marker tracking algorithm demonstrated the ability to follow markers with a velocity of 5 mm/s in the direction perpendicular to the slice orientation. This is expected, as the slice thickness equals 5 mm within the experiments, meaning the marker transitions between slices at a rate that aligns with the spatial resolution of the scanned volume. In theory, higher velocities are detectable in this direction. An example is shown in figure 7.1. When the center of the marker in the first iteration would be present in slice *#2*, the marker is detectable in the assessed slice subset of *#3, #4* and *#5*. If the marker would move 15 mm to slice *#5* within the next iteration (=1 second), then the marker is still detectable in the second iteration of slice subset *#2, #3* and *#4*. This example demonstrates that the maximum detectable velocity of the marker is 15 mm/s. However, this velocity is too high for continuous marker tracking.

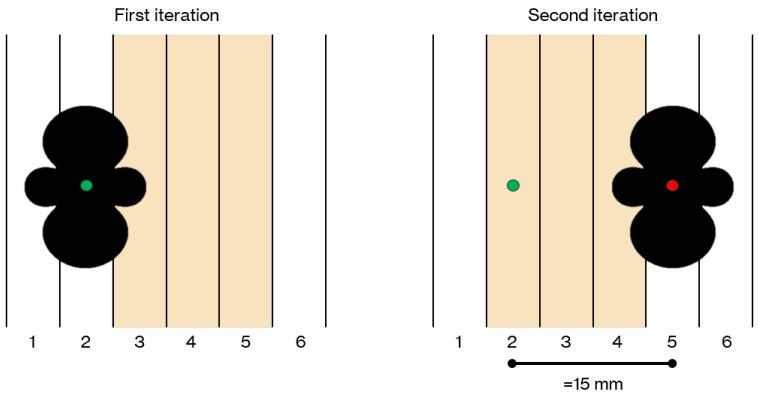

Figure 7.1: Schematic example of the maximum detectable marker velocity over one iteration.

Furthermore, when markers move within the plane of a slice, the CNN can handle significantly higher velocities. Since the nnUNet assesses the entire 2D area at once, the maximum velocity in these directions are limited by the FOV of the scanned image. For the experiments in this thesis, a maximum velocity would be equal to 160 (=pixels) x × 1.6 mm. In practice, these findings suggest that marker movement perpendicular to the slice orientation is limited by the slice thickness, while marker movement the slice is not. Therefore, in-plane marker movement could be automatically tracked with higher velocities.

7.2.3 Simulation

The dynamic experiment in the marker movement simulation showed promising results in terms of the performance of the automated marker tracking algorithm. The results indicate high accuracy, with deviations remaining within one voxel size in most cases. To be specific, while the voxel diagonal is equal to 5.5 mm, only the experiment where the marker moved a straight path at 4.5 mm/s resulted in a slightly higher deviation of 5.8 mm. However, when integrating the automated marker tracking algorithm in an iMRI workflow with real experimental MR-data, a greater deviation could be expected. This is likely due to the nnUNet performance in detecting simulated and real markers. When training the nnUNet, its dice score is calculated per fold based on a validation data that has simulated markers, just like the training data. Here, the nnUNet reached a dice score of 0.99, see figure 7.2. Table 5.3 presents the dice score of the nnUNet tested on a dataset with real scanned markers, which is 0.76. This difference may influence the performance of the algorithm's integration into the iMRI suite. Nevertheless, the performance analysis of the automated marker tracking algorithm proves that the algorithm itself performs effectively.

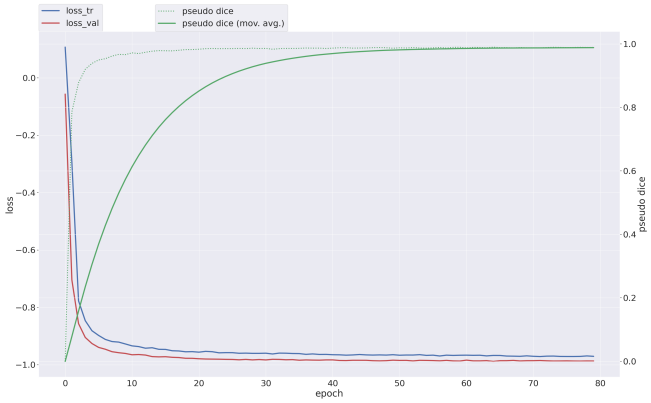

Figure 7.2: The training progress of nnUNet tested on validation data with simulated markers.

7.3 Future outlook

Throughout this thesis, several insights have been gained regarding automated passive marker tracking for iMRI. This section discusses some potential developments for future research.

7.3.1 Access-I

As the automated tracking algorithm was shown to work effectively within the developed closed-loop simulation with Python, the next step is to develop an experimental implementation within the iMRI suite. This can be done by using the Access-I module of the Siemens iMRI system. The implementation will allow for validating the automated tracking algorithm under realistic conditions. This can eventually establish iMRI

as a new image guidance modality for endovascular interventions. The developed simulation approach can continue to offer a convenient strategy for exploring new tracking options remotely.

7.3.2 Slice thickness

During scanning with the real-time TRUFI sequence, some challenges with respect to manually tracking the guidewire were identified. This had to do with maintaining precise spatial awareness of plane orientation within the 3D geometry. This unintuitive process highlighted the importance of this innovative automated tracking algorithm. By experimenting with parameters and adjusting the scan planes, it was found that the choice of slice thickness also impacts the ability to recognize the guidewire within the MRI scans. Scanning with thicker slices made the guidewire identification easier because the guidewire remains visible for a longer period upon movement, reducing discontinuities in its appearance. This observation suggests that modifying the slice thickness in real-time could serve as an additional strategy for improving guidewire tracking. Furthermore, increasing the slice thickness would also enable the automated marker tracking algorithm to detect markers with an increased velocity in the perpendicular direction of the slice orientation. However, increasing the slice thickness reduces the spatial resolution in that direction, which may be a drawback when scanning smaller structures such as arteries. Future research could explore the potential of adjusting the slice thickness as an additional degree of freedom for automated tracking.

7.3.3 Asymmetric markers

The passive markers used in this thesis have a defined symmetric shape. While this simplifies the production of the markers, it also limits the ability to detect the orientation of the markers. In future work, investigating the use of asymmetric markers could provide additional information about the spatial orientation of the markers. This could particularly be useful for clinical applications that require precise orientation of an endovascular device. In these procedures, it can be beneficial to recognize the tip orientation of the guidewire for maneuvering the catheter. Implementing asymmetric markers could enhance the recognition of the tip orientation and therefore potentially improve the accuracy and efficiency of the catheter guidance procedure.

7.3.4 Potential of slice angulation

As described in section 2.2.2, MRI is able to not only perform slice repositioning, but also slice angulation relative to B_0. As the appearances of the marker can already be simulated for any slice angle, the CNN can already detect these appearances. This capability presents new opportunities, as the slice can be freely oriented to ensure full appearance of the guidewire on the imaged slice. Slice angulation could also enable a navigation interface where clinicians could perform the procedure from a marker-centered perspective. Both possibilities could help clinicians navigate within an artery with improved spatial awareness.

7.3.5 Potential of preoperative information

To further enhance the spatial awareness and workflow of catheter guidance procedure, preoperative information from the patient could be integrated in the visualization software. The preoperative information could also be used to improve the marker detection by directing the detection process to preferential regions of interest. Another benefit from the preoperative information would be the ability for the clinicians to plan the intervention and optimize the procedure. Future research could investigate methods for combining real-time iMRI data with preoperative vascular models to enhance procedural planning and execution.

8 Conclusion

This thesis successfully established automated passive marker tracking for iMRI-guidance systems by the development of a nnUNet-based marker detection network and a slice repositioning algorithm.

The trained nnUNet demonstrated a strong detection performance and proved the feasibility of using deep learning for passive marker detection. Training the network with various marker orientations and positions improved the robustness of the nnUNet. While minor detection errors were observed, these concerned situations where the marker was in the adjacent slice or low-intensity regions near the silicone phantom border. These limitations are unlikely to affect clinical applications.

The slice repositioning algorithm is able to automatically update the slice position, following the marker position with a slight delay. This delay stemmed from processing time and small deviations introduced by the CNN's performance influencing the contour-based center detection. Improved estimation of the marker's center could enhance the tracking precision.

In addition, new opportunities are identified for the advancement of automated passive marker tracking with iMRI. The integration of the developed tracking algorithm into an iMRI system via the Access-I module would allow real-world validation under clinical conditions. Furthermore, exploring asymmetric markers could enable orientation detection of the guidewire tip, enhancing the guidance accuracy. Slice angulation techniques and the incorporation of preoperative imaging data could also further improve guidewire navigation and spatial awareness.

In conclusion, this thesis successfully demonstrated advancements for automated passive marker tracking for iMRI-guidance systems by combining a deep learning-based detection approach with automated slice repositioning techniques. This work represents an important step toward the adoption of iMRI as a guidance system for endovascular procedures, as the developed tracking algorithm improves the clinical workflow for MR-guided procedures. Further research should focus on refining the precision and robustness of automated marker tracking solution and integrating the solution into iMRI suite to improve the performance of endovascular procedures.

Bibliography

1. Nijsink H, Overduin CG, Willems LH, Warlé MC, and Fütterer JJ. Current State of MRI-Guided Endovascular Arterial Interventions: A Systematic Review of Preclinical and Clinical Studies. Journal of Magnetic Resonance Imaging 2022 Nov; 56:1322–42. DOI: 10.1002/jmri.28205
2. Tang QH, Chen J, Hu CF, and Zhang XL. Comparison Between Endovascular and Open Surgery for the Treatment of Peripheral Artery Diseases: A Meta-Analysis. 2020 Jan. DOI: 10.1016/j.avsg.2019.06.039
3. Akkus NI, Mina GS, Abdulbaki A, Shafiei F, and Tandon N. Using 7.5 frames per second reduces radiation exposure in lower extremity peripheral vascular interventions. Vascular 2015 Jun; 23:240–4. DOI: 10.1177/1708538114549592. Available from: https://pubmed.ncbi.nlm.nih.gov/25208902/
4. Sciahbasi A, Ferrante G, Fischetti D, Miklin DJ, Sarandrea A, Schirripa V, Guarracini F, Arya A, Loreni G, Bruni A, Rigattieri S, Marini M, Vagnarelli S, Scevola G, Reimers B, Hindricks G, and Cohen M. Radiation dose among different cardiac and vascular invasive procedures: The RODEO study. International Journal of Cardiology 2017 Aug; 240:92–6. DOI: 10.1016/j.ijcard.2017.03.031. Available from: https://www.internationaljournalofcardiology.com/action/showFullText?pii=S0167527317309683%20https://www.internationaljournalofcardiology.com/action/showAbstract?pii=S0167527317309683%20https://www.internationaljournalofcardiology.com/article/S0167-5273(17)30968-3/abstract
5. Mislow JM, Golby AJ, and Black PM. Origins of Intraoperative MRI. Neurosurgery clinics of North America 2009 Apr; 20:137. DOI: 10.1016/J.NEC.2009.04.002. Available from: https://pmc.ncbi.nlm.nih.gov/articles/PMC2902263/
6. Wang W. MR Guided Active Catheter Tracking. Magnetic resonance imaging clinics of North America 2015 Nov; 23:579. DOI: 10.1016/J.MRIC.2015.05.009. Available from: /pmc/articles/PMC4621764/%20https://www.ncbi.nlm.nih.gov/pmc/articles/PMC4621764/
7. Rogers T, Campbell-Washburn AE, Ramasawmy R, Yildirim DK, Bruce CG, Grant LP, Stine AM, Kolandaivelu A, Herzka DA, Ratnayaka K, and Lederman RJ. Interventional cardiovascular magnetic resonance: state-of-the-art. Journal of Cardiovascular Magnetic Resonance 2023 Dec; 25:48. DOI: 10.1186/S12968-023-00956-7. Available from: /pmc/articles/PMC10424337/%20/pmc/articles/PMC10424337/?report=abstract%20https://www.ncbi.nlm.nih.gov/pmc/articles/PMC10424337/
8. Reinok M, Dagnino G, and Brink W. Automated Passive Tracking for MR-guided Endovascular Interventions. Tech. rep.
9. Antoniou GA, Antoniou SA, and Torella F. Editor's Choice – Endovascular vs. Open Repair for Abdominal Aortic Aneurysm: Systematic Review and Meta-analysis of Updated Peri-operative and Long Term Data of Randomised Controlled Trials. European Journal of Vascular and Endovascular Surgery 2020 Mar; 59:385–97. DOI: 10.1016/j.ejvs.2019.11.030. Available from: https://www.ejves.com/action/showFullText?pii=S1078588419326243%20https://www.ejves.com/action/showAbstract?pii=S1078588419326243%20https://www.ejves.com/article/S1078-5884(19)32624-3/abstract
10. Jerry L. Prince and Jonathan M. Links. Medical_Imaging_Signals_and_Systems. *Medical Imaging Signals and Systems*. 2015 :407–98

11. Campbell-Washburn AE, Tavallaei MA, Pop M, Grant EK, Chubb H, Rhode K, and Wright GA. Real-time MRI guidance of cardiac interventions. Journal of Magnetic Resonance Imaging 2017 Oct; 46:935–50. DOI: 10.1002/jmri.25749
12. Nayak KS, Lim Y, Campbell-Washburn AE, and Steeden J. Real-Time Magnetic Resonance Imaging. Journal of magnetic resonance imaging : JMRI 2022 Jan; 55:81–99. DOI: 10.1002/JMRI.27411. Available from: https://pubmed.ncbi.nlm.nih.gov/33295674/
13. Nijsink H, Overduin CG, Brand P, De Jong SF, Borm PJ, Warlé MC, and Fütterer JJ. Optimised passive marker device visibility and automatic marker detection for 3-T MRI-guided endovascular interventions: a pulsatile flow phantom study. European Radiology Experimental 2022 Dec; 6. DOI: 10.1186/s41747-022-00262-4
14. Basar B, Sonmez M, Yildirim DK, Paul R, Herzka DA, Kocaturk O, Lederman RJ, and Campbell-Washburn AE. Susceptibility artifacts from metallic markers and cardiac catheterization devices on a high-performance 0.55 T MRI system. Magnetic Resonance Imaging 2021 Apr; 77:14–20. DOI: 10.1016/J.MRI.2020.12.002. Available from: https://www.researchgate.net/publication/347910452_Susceptibility_artifacts_from_metallic_markers_and_cardiac_catheterization_devices_on_a_high-performance_055_T_MRI_system
15. Yildirim DK, Uzun D, Bruce CG, Khan JM, Rogers T, Schenke WH, Ramasawmy R, Campbell-Washburn A, Herzka DA, Lederman RJ, and Kocaturk O. An interventional MRI guidewire combining profile and tip conspicuity for catheterization at 0.55T. Magnetic resonance in medicine 2023 Feb; 89:845–58. DOI: 10.1002/MRM.29466. Available from: https://pubmed.ncbi.nlm.nih.gov/36198118/
16. Bock M, Müller S, Zuehlsdorff S, Speier P, Fink C, Hallscheidt P, Umathum R, and Semmler W. Active catheter tracking using parallel MRI and real-time image reconstruction. Magnetic resonance in medicine 2006; 55:1454–9. DOI: 10.1002/MRM.20902. Available from: https://pubmed.ncbi.nlm.nih.gov/16683261/
17. Settecase F, Martin AJ, Lillaney P, Losey A, and Hetts SW. MR-guided Passive Catheter Tracking for Endovascular Therapy. Magnetic resonance imaging clinics of North America 2015 Nov; 23:591. DOI: 10.1016/J.MRIC.2015.05.003. Available from: /pmc/articles/PMC4621770/%20/pmc/articles/PMC4621770/?report=abstract%20https://www.ncbi.nlm.nih.gov/pmc/articles/PMC4621770/
18. Clogenson HC and Van Den Dobbelsteen JJ. Catheters and Guidewires for Interventional MRI: Are We There Yet? Catheters and guide wires for interventional MRI: are we there yet? Imaging Med 2016; 8. Available from: https://www.researchgate.net/publication/303868538
19. MR-capable medical devices. Available from: https://www.epflex.com/en/products/mrline/
20. Seppenwoolde JH, Viergever MA, and Bakker CJ. Passive tracking exploiting local signal conservation: the white marker phenomenon. Magnetic resonance in medicine 2003 Oct; 50:784–90. DOI: 10.1002/MRM.10574. Available from: https://pubmed.ncbi.nlm.nih.gov/14523965/
21. Zijlstra F, Viergever MA, and Seevinck PR. SMART tracking: Simultaneous anatomical imaging and real-time passive device tracking for MR-guided interventions. Physica Medica 2019 Aug; 64:252–60. DOI: 10.1016/J.EJMP.2019.07.019
22. Gassenmaier S, Küstner T, Nickel D, Herrmann J, Hoffmann R, Almansour H, Afat S, Nikolaou K, and Othman AE. Deep Learning Applications in Magnetic Resonance Imaging: Has the Future Become Present? Diagnostics 2021 Dec; 11. DOI: 10.3390/DIAGNOSTICS11122181. Available from: /pmc/articles/PMC8700442/%20/pmc/articles/PMC8700442/?report=abstract%20https://www.ncbi.nlm.nih.gov/pmc/articles/PMC8700442/
23. Lundervold AS and Lundervold A. An overview of deep learning in medical imaging focusing on MRI. Zeitschrift für Medizinische Physik 2019 May; 29:102–27. DOI: 10.1016/J.ZEMEDI.2018.11.002
24. Zhang A, Lipton ZC, Li M, and Smola AJ. Dive into Deep Learning. Journal of the American College of Radiology 2021 Jun; 17:637–8. DOI: 10.1016/j.jacr.2020.02.005. Available from: https://arxiv.org/abs/2106.11342v5
25. Dou Q, Chen H, Yu L, Zhao L, Qin J, Wang D, Mok VC, Shi L, and Heng PA. Automatic Detection of Cerebral Microbleeds From MR Images via 3D Convolutional Neural Networks. IEEE transactions on medical imaging 2016 May; 35:1182–95. DOI: 10.1109/TMI.2016.2528129. Available from: https://pubmed.ncbi.nlm.nih.gov/26886975/

26. Grøvik E, Yi D, Iv M, Tong E, Rubin D, and Zaharchuk G. Deep Learning Enables Automatic Detection and Segmentation of Brain Metastases on Multisequence MRI. Journal of magnetic resonance imaging : JMRI 2020 Jan; 51:175. DOI: 10.1002/JMRI.26766. Available from: /pmc/articles/PMC7199496/%20/pmc/articles/PMC7199496/?report=abstract%20https://www.ncbi.nlm.nih.gov/pmc/articles/PMC7199496/
27. Bos C, Viergever MA, and Bakker CJ. On the artifact of a subvoxel susceptibility deviation in spoiled gradient-echo imaging. Magnetic Resonance in Medicine 2003 Aug; 50:400–4. DOI: 10.1002/mrm.10505
28. Schenck JF. The role of magnetic susceptibility in magnetic resonance imaging: MRI magnetic compatibility of the first and second kinds. Medical physics 1996; 23:815–50. DOI: 10.1118/1.597854. Available from: https://pubmed.ncbi.nlm.nih.gov/8798169/
29. Rodrigues O. Des lois géométriques qui régissent les déplacements d'un système solide dans l'espace, et de la variation des coordonnées provenant de ces déplacements considérés indépendamment des causes qui peuvent les produire. Journal de Mathématiques Pures et Appliquées 1840; 5:380–440. Available from: http://www.numdam.org/item?id=JMPA_1840_1_5__380_0
30. Isensee F, Jaeger PF, Kohl SA, Petersen J, and Maier-Hein KH. nnU-Net: a self-configuring method for deep learning-based biomedical image segmentation. Nature Methods 2020 18:2 2020 Dec; 18:203–11. DOI: 10.1038/s41592-020-01008-z. Available from: https://www.nature.com/articles/s41592-020-01008-z
31. MONAI - Home. Available from: https://monai.io/
32. F-score | Definition, Formula, & Facts | Britannica. Available from: https://www.britannica.com/science/F-score
33. Dice score - OECD.AI. Available from: https://oecd.ai/en/catalogue/metrics/dice-score

Appendix A: Slice repositioning

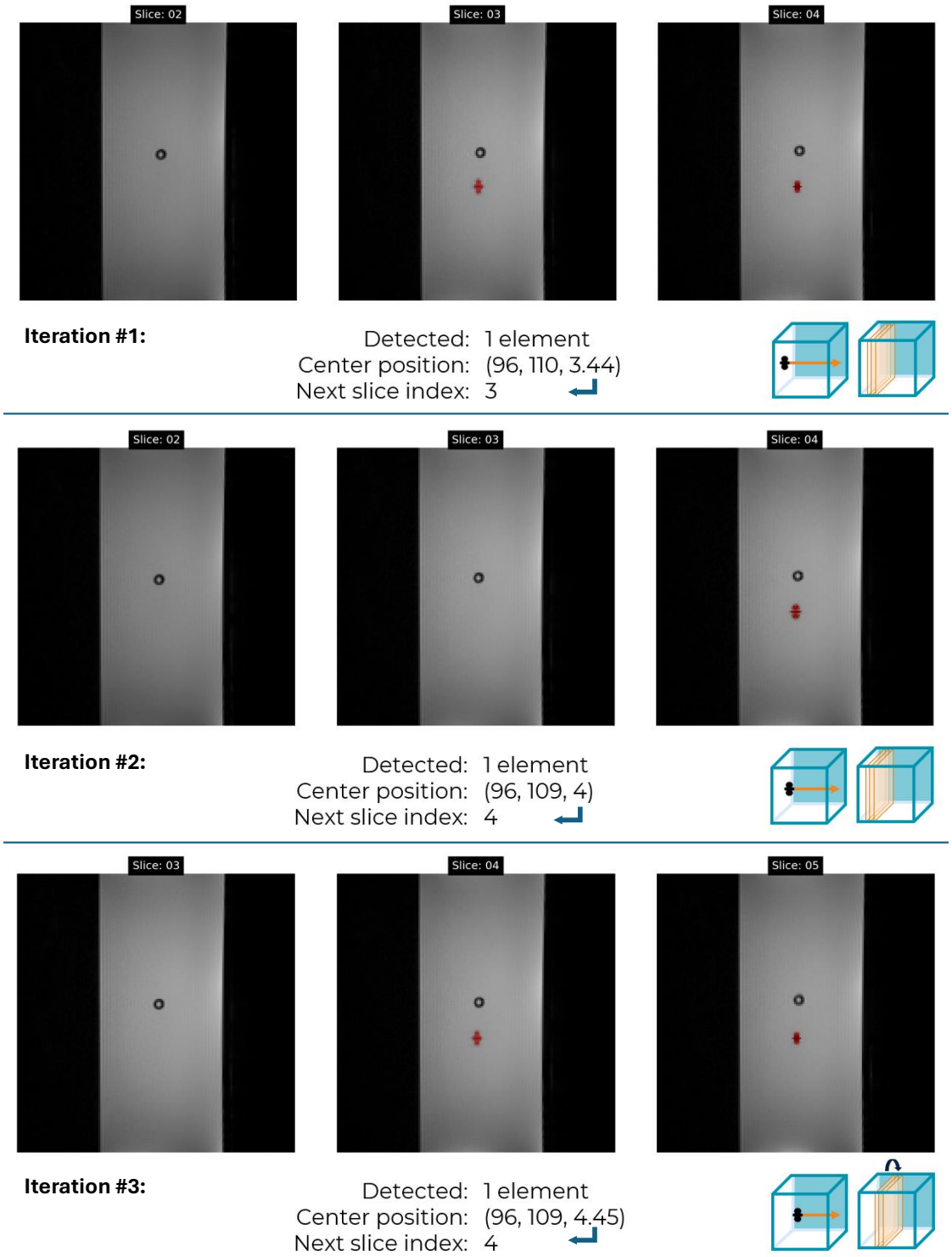

Figure A.1: An example of setting the new center slice index by the automated passive marker tracking algorithm.

Appendix B: Tracked paths for trajectories

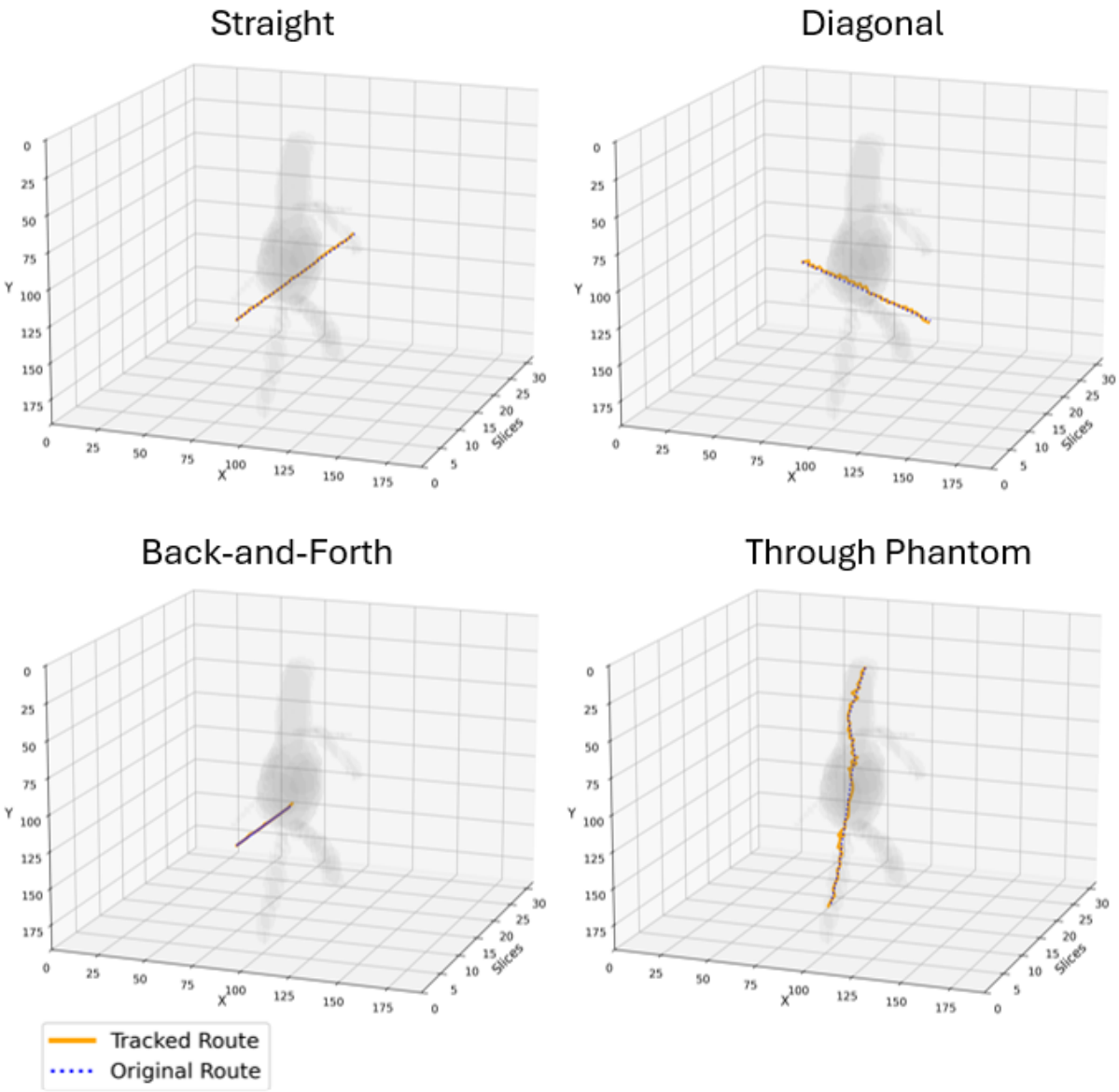

Figure B.1: Plots of the tracked routes of the passive marker by the automated 3D tracking algorithm compared to the original routes of the passive marker for all four trajectories.

Appendix C: RMSE distribution

C.1 Trajectories:

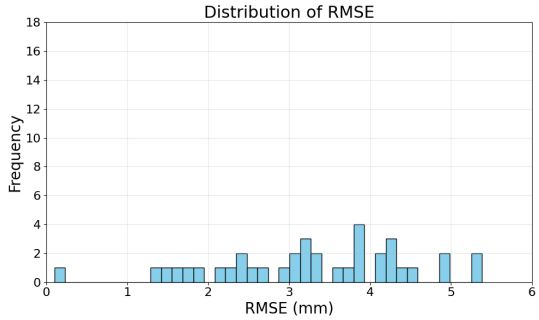

(a) Straight trajectory

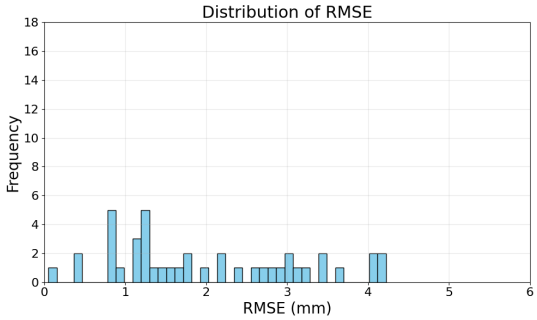

(b) Diagonal trajectory

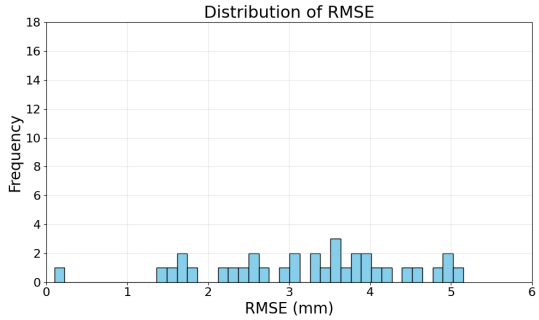

(c) Back-and-forth trajectory

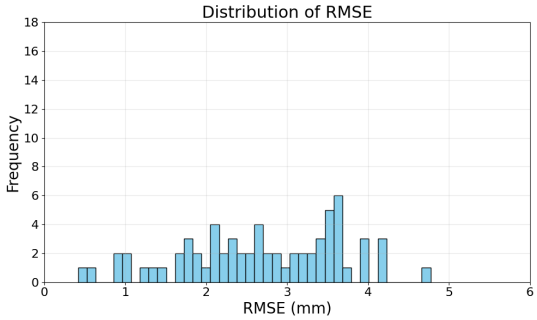

(d) Through phantom trajectory

Figure C.1: A visualization of the distribution of the RMS errors of the predicted and true center coordinates of the dynamic simulation for the different trajectories.

C.2 Velocities:

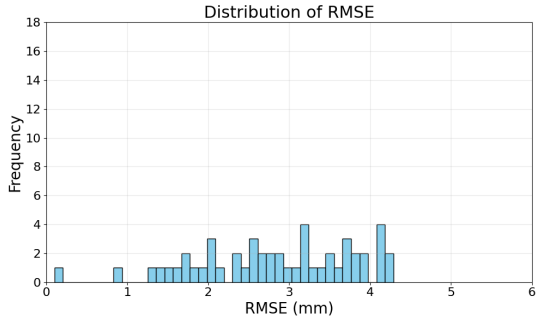

(a) 3 mm/s

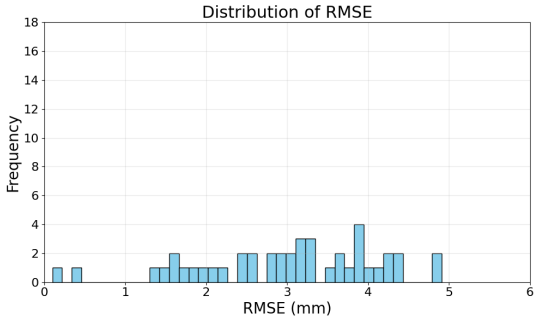

(b) 3.5 mm/s

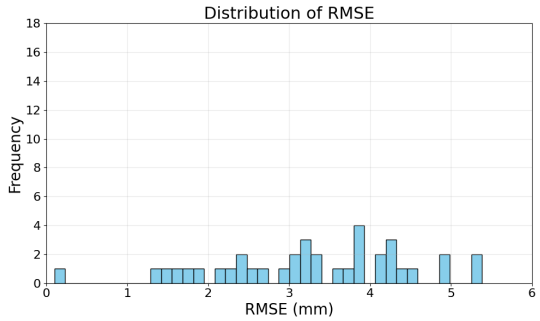

(c) 4 mm/s

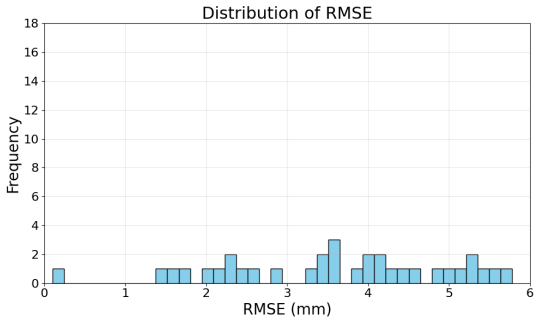

(d) 4.5 mm/s

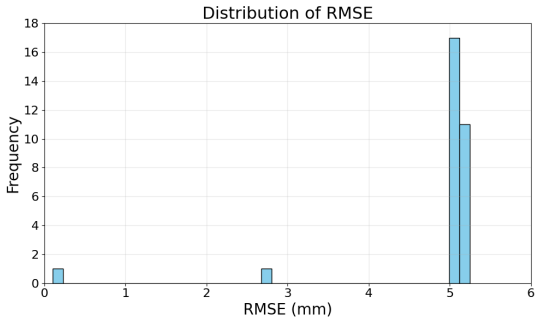

(e) 5 mm/s

Figure C.2: A visualization of the distribution of the RMS errors of the predicted and true center coordinates of the dynamic simulation for the different velocities.

Appendix D: Deviation per dimension

D.1 Trajectories:

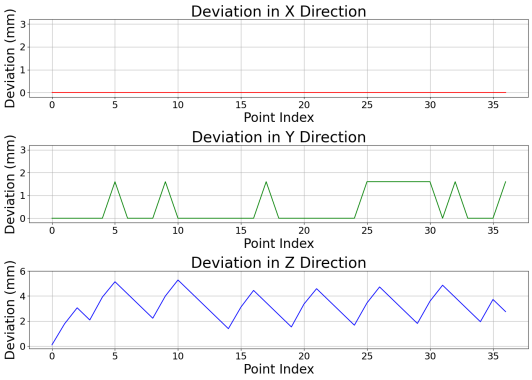

(a) Straight trajectory

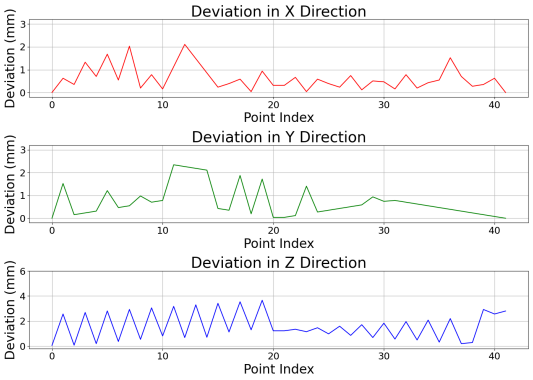

(b) Diagonal trajectory

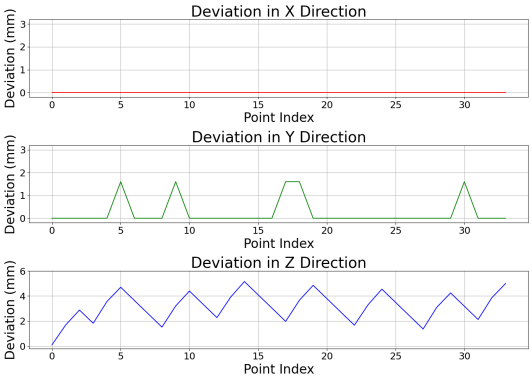

(c) Back-and-forth trajectory

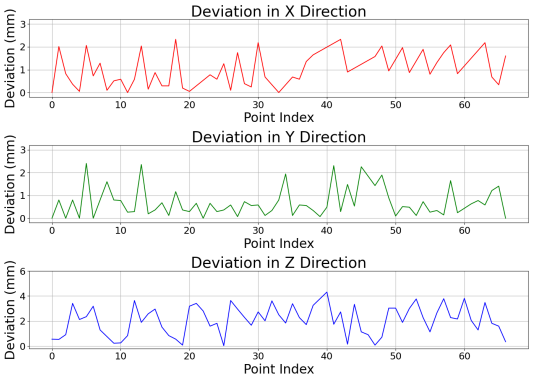

(d) Through phantom trajectory

Figure D.1: A visualization of the deviation between the predicted and true center coordinates per direction of the dynamic simulation for the different trajectories.

D.2 Velocities:

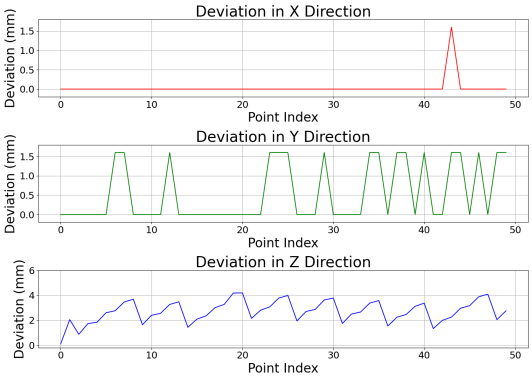

(a) 3 mm/s

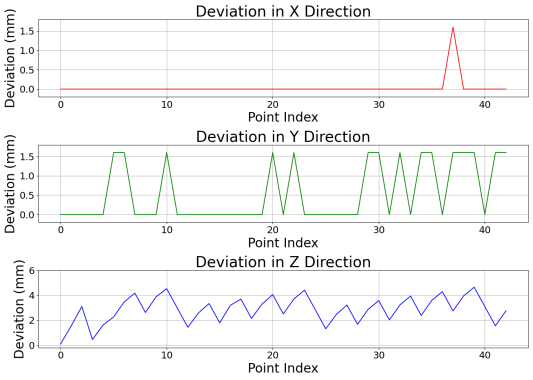

(b) 3.5 mm/s

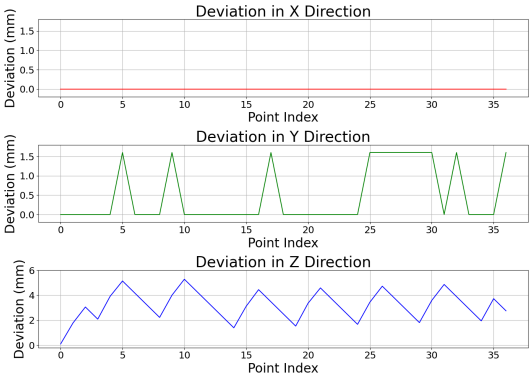

(c) 4 mm/s

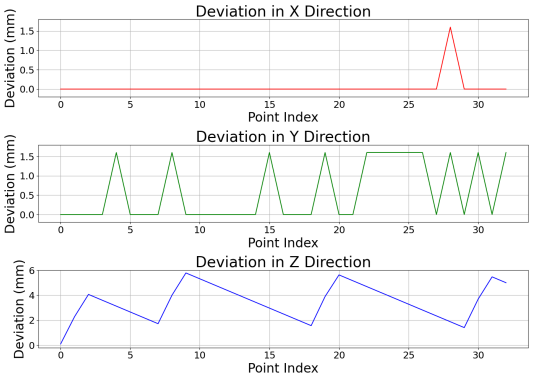

(d) 4.5 mm/s

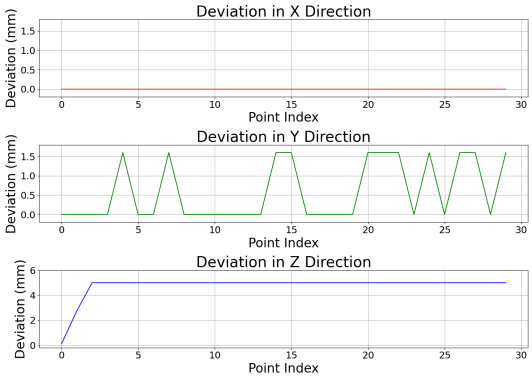

(e) 5 mm/s

Figure D.2: A visualization of the deviation between the predicted and true center coordinates per direction of the dynamic simulation for the different velocities.